Reviews of Modern Plasma Physics (2022) 6:25
https://doi.org/10.1007/s41614-022-00088-y

SPECIAL TOPICS

Study of Alfvén eigenmodes with heavy ion beam probing in the TJ-II stellarator

L. G. Eliseev[1] · A. V. Melnikov[1,2,3] · S. E. Lysenko[1]

Received: 30 March 2022 / Accepted: 12 August 2022 / Published online: 5 September 2022

Abstract

The study of Alfvén eigenmodes (AEs) driven by fast particles in toroidal plasmas is of a great importance for future fusion reactor with plasma, dominating by fusion alphas. The review is the first attempt to describe systematically AEs in the TJ-II stellarator with low magnetic shear, and to summarize more than 10 years of the direct application of the Heavy Ion Beam Probing (HIBP)—a diagnostic with unique capabilities to study AEs in toroidal plasmas by local measurement of the AE-excited electric potential and density perturbation in the plasma core along with magnetic potential perturbations. Experimental findings, including absolute values of plasma potential and density perturbation, and the mode radial location, are compared with numerical simulations that allows us to identify the observed modes as helicity induced Alfvén eigenmodes (HAE) and global Alfvén eigenmodes (GAE). On top of that, the mode poloidal rotation, mode numbers, and turbulent particle flux estimations are described. 2D poloidal map of the AEs demonstrates the ballooning character of plasma potential perturbation. AEs in both continuous frequency and chirping form shows strong evolution caused by rotational transform (iota) change, the suggested analytical model for the mode frequency describes the observation. AE frequency dynamics down to geodesic acoustic mode frequency with iota variation along with AE transformation from continuous to chirping form and back is observed.

Keywords Alfvén eigenmodes · TJ-II stellarator · HIBP

✉ A. V. Melnikov
melnikov_07@yahoo.com

[1] National Research Center 'Kurchatov Institute', Moscow, Russia 123182

[2] National Research Nuclear University MEPhI, Moscow, Russia 115409

[3] Moscow Institute of Physics and Technology, Moscow Region, Dolgoprudny, Russia 141700

1 Introduction

Investigation of Alfvén eigenmodes (AEs) induced by energetic particles in toroidal plasmas is of a great importance for future fusion reactors, where plasma is mainly heated by fusion alphas and beams of energetic ions from neutral beam injection (NBI) and ion-cyclotron resonance frequency (ICRF) heating. A theory predicts that AEs could cause additional losses of the fast ions in modern fusion devices, and could potentially impede the proper operation of future fusion reactors like ITER (Heidbrink 2008; Fasoli et al. 2007).

Alfvén waves were proposed by Hannes Alfvén in the 1942 for the space plasmas (Alfvén 1942). Alfvén waves propagate along magnetic field lines with a velocity $V_A \propto B_t\, n_e^{-1/2}$. In magnetic fusion devices, the magnetic field has periodic structure with ripples that set up the multiple resonance conditions for Alfvén waves, therefore, they form various types of eigenmodes, called as Alfvén eigenmodes (AEs). AEs are extensively studied in both modern tokamaks and stellarators mainly with conventional diagnostics, see reviews (Gorelenkov et al. 2014; Breizman and Sharapov 2011; Toi et al. 2011).

Numerical gyrokinetic simulations show that energetic particles may nonlinearly interact with various types of turbulence such as ITG and TEM instabilities, and with zonal flows (Hidalgo et al. 2022; Liu et al. 2022; Siena et al. 2019a). The high-frequency counterpart of zonal flows, geodesic acoustic modes (GAMs) are considered as a mechanism for the self-regulation of turbulence in toroidal plasmas: broadband turbulence generates GAM, which in turn suppresses the turbulence (Diamond et al. 2005). There were experimental evidences of the three-wave coupling between GAM and broadband turbulence with HIBP (Melnikov et al. 2017a; Gryaznevich et al. 2020; Riggs et al. 2021). The theory predicts that GAMs and AEs are different branches of the common dispersion relation (Conway et al. 2022), and there are consistent experimental evidences of the links between GAMs and AEs (Zeeland et al. 2016; Breizman et al. 2005; Toi et al. 2010).

Alfvén instabilities driven by fast ion in the low-density TJ-II plasmas are frequently observed as chirping modes with bursting amplitudes and up-sweeping frequencies in the range 100–350 kHz (Nagaoka et al. 2013; Melnikov et al. 2010a; Garcia-Munoz et al. 2019; Yamamoto et al. 2020). Effect of chirping modes on fast ions may differ from the one of the conventional steady-frequency AEs. They may change the character of energetic ion losses from diffusive to convective ones. At higher densities, in NBI-only heated plasmas, both chirping and continuous modes in the range 50–300 kHz were observed (Melnikov et al. 2012; Jiménez-Gómez et al. 2011). The TJ-II is very relevant to study AEs, because it has a low magnetic shear—the key feature of advanced tokamak scenario for fusion reactors. So TJ-II configurations are of interest as a laboratory model for AE features in the vicinity of the reversal of magnetic shear. Also TJ-II possess exclusive diagnostic–double multichannel Heavy Ion Beam Probe (HIBP) (Melnikov et al. 2017b), which recently becomes the multi-purpose diagnostics, providing simultaneous information about the mean values and fluctuations of the local electric potential φ from the beam

energy E_b, electron density n_e from the beam current I_t, and magnetic potential A_ζ (or poloidal magnetic field $B_{\rm pol}$) from the toroidal beam shift ζ.

This review summarizes the main results of studying AEs with HIBP in TJ-II. In Sect. 2, we briefly discuss the main features of TJ-II. In Sect. 3, we discuss physical principles of HIBP measurements and implementation of HIBP in AE on TJ-II including its advantages and drawbacks. Section 4 presents the results AE observations: the time evolution, radial localization and poloidal rotation of AE, the frequency spectrum and its dependence on the magnetic configuration. In Sect. 5, we describe observations a lower limit of AE frequency linked to a Geodesic acoustic mode (GAM) frequency and compare experimental results with analytical and numerical simulations. Section 6 discusses the turbulent particle flux associated to AE. In Sect. 7, we discuss 2D maps of AE. Section 8 describes the chirping modes and considers AE transformation from continuous frequency form to the chirping and back. The key novel findings about AE physics are summarized in Sect. 9. The outstanding issues in HIBP diagnostic and in AE physics, including the directions for future work are presented in Sect. 10.

2 The TJ-II stellarator

TJ-II is a heliac type stellarator with averaged major radius $R=1.5$ m, averaged minor radius $a\leq 0.22$ m, four periods, average magnetic field on axis $B_t=0.95$ T, plasma volume ≤ 1 m^3. Plasma is produced, heated and sustained by either electron–cyclotron resonance heating (ECRH) with two gyrotrons, operating at 53.2 GHz, $P_{\rm EC}\leq 300$ kW each, or neutral beam injection (NBI) with two H_0 injectors, $E_{\rm NBI}\leq 32$ keV, $P_{\rm NBI}\leq 600$ kW each; H^+ ions with velocity $V_{\rm NBI}\sim 2.5\times 10^6$ m/s, which is about 1/3 of the Alfvén velocity V_A:

$$V_A = \frac{B}{\sqrt{\mu_0 \sum_i n_i m_i}}. \tag{1}$$

The AE frequency is defined by Alfvén law:

$$f_{\rm AE} = \frac{1}{2\pi} k_\parallel V_A, \tag{2}$$

where the mode wave-vector is

$$k_{||} = \frac{1}{R}|m\iota - n|. \tag{3}$$

Here n_i is particle density, m_i is particle mass, m and n are toroidal and poloidal numbers. Vacuum magnetic configuration or rotational transform $\iota_{\rm vac}$ is regulated by currents $I_{\rm CC}$, $I_{\rm HX}$ and $I_{\rm VF}$ in the magnetic coils CC, HX and VF shown in Fig. 1a. Each configuration is marked by these currents in kA/10, e.g. in the standard configuration 100_44_64. These currents may be changed independently, this way TJ-II may vary vacuum rotational transform $\iota_{\rm vac}$ from shot to shot in the wide range: $0.9<\iota_{\rm vac}(0)<2.5$. TJ-II is characterized by low magnetic shear, the vacuum iota

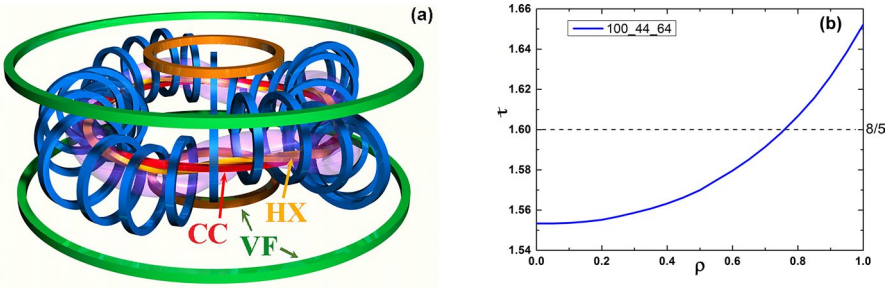

Fig. 1 **a** Magnetic system of TJ-II. Plasma column is pink, toroidal field coils are blue. Helical coil (HX), circular coil (CC) and vertical field coils (VF) are used for the magnetic configuration control (Melnikov et al. 2004). Reproduced courtesy of IAEA. **b** Vacuum iota for the standard magnetic configuration. The low-order rational magnetic surface $n/m = 8/5$ is shown by dash line

profile in the standard configuration is shown in Fig. 1b. Actual magnetic configuration ι is affected by plasma current up to several kA ($\iota = 1/q$, q is the safety factor in tokamaks). Figure 2 is the photo of TJ-II, and Fig. 3 shows location of sources of NBI and ECR heating, and positions of several diagnostics. The main TJ-II findings in the fields of AEs, plasma potential and turbulence obtained with HIBP contribution are presented in Hidalgo et al. (2022), Melnikov et al. (2007), Melnikov et al. (2011), Sánchez et al. (2013), Sánchez et al. (2015), Castejon et al. (2016), Castejón et al. (2017), Ascasibar et al. (2019) and Melnikov et al. (2014).

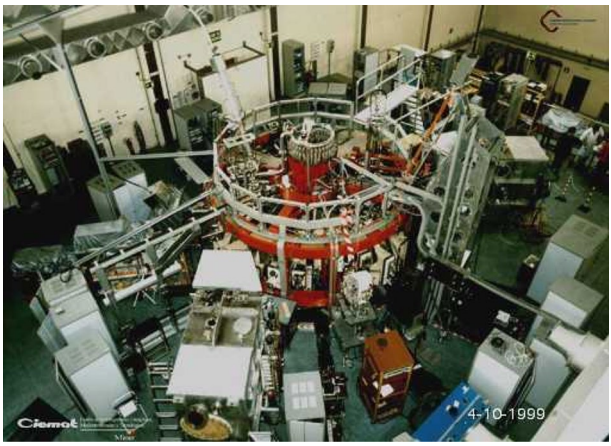

Fig. 2 General view of TJ-II

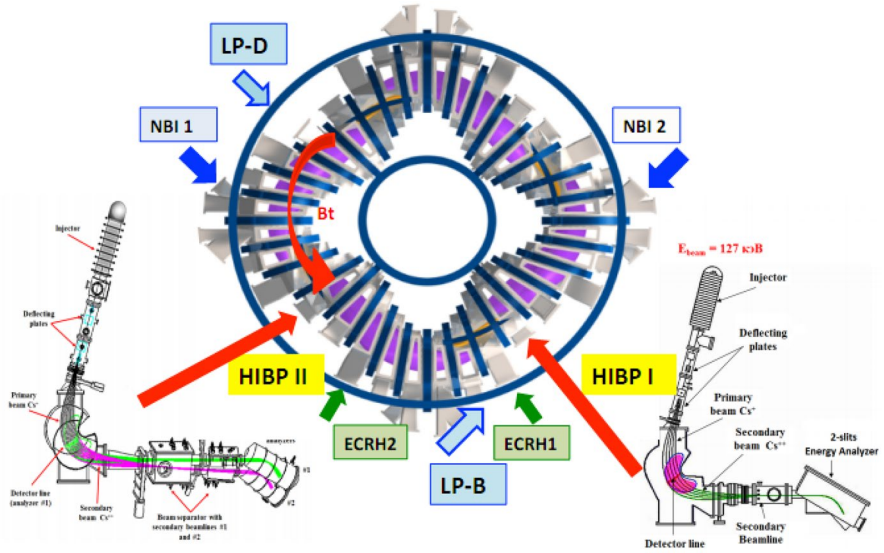

Fig. 3 TJ-II top view: ECRH1, 2 are gyrotrons, 2×300 kW; NBI 1, 2 are co- and counter-injectors, 2×500 kW; HIBP I, II is the dual system; LP-B, D are two system of Langmuir probes (Hidalgo et al. 2022). Reproduced courtesy of IAEA

3 HIBP diagnostic—a versatile tool to study AE

The heavy ion beam probe (HIBP) has unique capabilities to study fusion plasmas (Dnestrovskij et al. 1994). HIBP was first used in 1960s by R. Hickok and F. Jobes in the arc discharge and later in the ST tokamak (Jobes and Hickok 1970). The world-wide status of HIBP diagnostic development up to 1993 is described in the Special issue of IEEE Trans. Plasma Sci. devoted to Hickok (Many authors 1994).

For the first time in USSR (now Russia), HIBP was implemented by Krupnik and Nedzelskiy (Kharkov, Ukraine) to the TM-4 tokamak in Kurchatov Institute in 1980s (Bugarya et al. 1983, 1985). For the moment, HIBP is the only method allowing non-disturbing direct measurements of the electric potential in a hot plasma core (Melnikov et al. 2017b). Figure 4 shows the principal scheme of HIBP with split-plate beam detector, used in the T-10 tokamak (Melnikov et al. 1995, 2019) and in the TJ-II stellarator (Melnikov et al. 2015).

The HIBP measurements of electric potential are based on the energy conservation of the probing particle moving along the Larmor orbit in the 3D magnetic field of a fusion device (Melnikov 2019). A primary ion beam with energy E_b enters the plasma. At the secondary ionization point in the plasma, or sample volume (SV), a beam ion loses an electron. Its potential energy $-e\varphi_{\rm pl}^{\rm SV}$ goes to a secondary, doubly charged ion. The total energy of the secondary ion leaving the plasma is $E_d = E_b + e\varphi_{\rm pl}^{\rm SV}$. So, the local potential at SV is $\varphi_{\rm pl}^{\rm SV} = (E_d - E_b)/e$, where E_b is a known constant, E_d is measured by the energy analyser. HIBP in TJ-II uses the

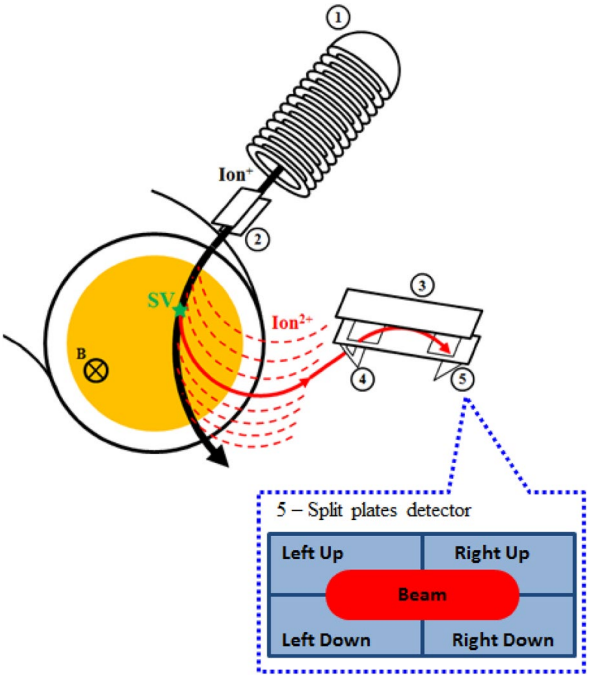

Fig. 4 The scheme of HIBP diagnostic. (1)—Injector, (2)—Sweeping plates; (3)—Parallel plate energy analyzer; (4)—its entrance slit; (5)—Detector plates; SV—Sample volume; *B*—toroidal magnetic field. The fat black line is the orbit of primary beam, red lines are orbits of secondary beams

parallel plate conventional energy analyzer with voltage U_{an}, dynamic factor F and gain G (Bondarenko et al. 2001), so for plasma potential we have

$$\varphi = 2U_{\mathrm{an}}(F\,\delta i + G) - U_{\mathrm{b}}, \tag{4}$$

where U_b is accelerating voltage, δi is vertical normalized difference of the beam currents at the detector plates: Left (L), Right (R), Up (U) and Down (D):

$$\delta i = \frac{i_{\mathrm{LU}} + i_{\mathrm{RU}} - i_{\mathrm{LD}} - i_{\mathrm{RD}}}{i_{\mathrm{LU}} + i_{\mathrm{RU}} + i_{\mathrm{LD}} + i_{\mathrm{RD}}}, \tag{5}$$

representing the beam position along the electric field of the analyser or vertical position.

The total secondary beam current:

$$I_{\mathrm{t}} = i_{\mathrm{LU}} + i_{\mathrm{RU}} + i_{\mathrm{LD}} + i_{\mathrm{RD}} \tag{6}$$

is proportional to the local plasma density in the SV, $n_{\mathrm{e}}^{\mathrm{SV}}$, and the relative density fluctuations are

$$\delta n_{\mathrm{e}}(\rho,t)/n_{\mathrm{e}}(\rho,t) = \tilde{I}_{\mathrm{t}}(\rho,t)/\bar{I}_{\mathrm{t}}(\rho), \tag{7}$$

where $\tilde{I}_t$ and $\bar{I}_t$ are fluctuating and mean values of I_t, but at high densities we should take into account the beam attenuation along the trajectory (Khabanov et al. 2019). In this case, $n_{\mathrm{e}}^{\mathrm{SV}}$ is linked with I_t by the integral equation:

$$I_t(\rho,t) = 2I_b n_e^{SV}(\rho,t)\sigma^{12}\lambda \times \exp\left(-\int_{L_1(\rho)} n_e(s)\sigma^{12}(s)ds - \int_{L_2(\rho)} n_e(s)\sigma^{23}(s)\mathrm{d}s\right), \tag{8}$$

where I_b is the initial primary beam current, σ^{12} and σ^{23} are the effective cross-sections for electron impact ionization for primary and secondary ions, λ is the SV length. Two integrals along the primary $L_1(\rho)$ and the secondary $L_2(\rho)$ trajectories show attenuations of the primary and secondary beams, ρ is the SV's normalized minor radius, dimensionless label of the flux surface.

The beam displacement in the toroidal direction ζ:

$$\zeta = \frac{i_{\mathrm{LU}} - i_{\mathrm{RU}} + i_{\mathrm{LD}} - i_{\mathrm{RD}}}{i_{\mathrm{LU}} + i_{\mathrm{RU}} + i_{\mathrm{LD}} + i_{\mathrm{RD}}} = \delta B_{\mathrm{pol}}/B_{\mathrm{pol}} \tag{9}$$

or beam horizontal normalized difference, caused by poloidal magnetic field B_{pol}, is used for internal magnetic measurements.

The integral equation for the oscillatory component of magnetic potential $A_{\zeta\mathrm{SV}}$, or for the poloidal magnetic flux $\psi_{\mathrm{SV}} = A_{\zeta\mathrm{SV}} R_{\mathrm{SV}}$ is following (Melnikov et al. 2017b):

$$\begin{aligned}\delta\zeta = {} & \delta\psi_{\mathrm{SV}}/m_b \int_{L_2} \mathrm{d}l/R^2 - 1/m_b \int_{L_1} \delta\psi \mathrm{d}l/R^2 \\ & - 2/m_b \int_{L_2} \delta\psi \mathrm{d}l/R^2 + P_{\zeta\mathrm{inj}}/m_b \int_{L_1} \delta\psi \mathrm{d}l/R^2 + \zeta_{\mathrm{inj}}.\end{aligned} \tag{10}$$

Here $A_{\zeta d}$ and $P_{\zeta\mathrm{inj}}$ are known constants, determined by the coordinates of injector and detector and by initial toroidal beam velocity; R_{SV} and R_d are the major radii of the sample volume and detector, m_b is probing ion mass.

Note that measurements of mean plasma potential and its fluctuations are always local, while measurements of density and magnetic fluctuations may be complicated by the path integral effect. In the TJ-II low-density plasmas, this effect for density fluctuations is not so prominent, but it should be accounted for magnetic fluctuations (Weisen et al. 2011; Melnikov et al. 2016a).

We develop the procedure for the density profile reconstruction from HIBP data (Khabanov et al. 2019), which takes into account the beam attenuation at high densities and the temperature dependence of cross-sections σ^{12} and σ^{23} in Eq. (8) for beam current. For normalization, we use the line-average density measured by the interferometer. Figure 5 shows comparison of density profiles measured by HIBP and by laser Thomson scattering (TS). HIBP has many advantages relative TS, because in TJ-II laser fires one time per discharge and covers only the central part of plasma ($\rho < 0.6$), while HIBP covers almost the whole cross-section and gives up to 40 profiles per discharge.

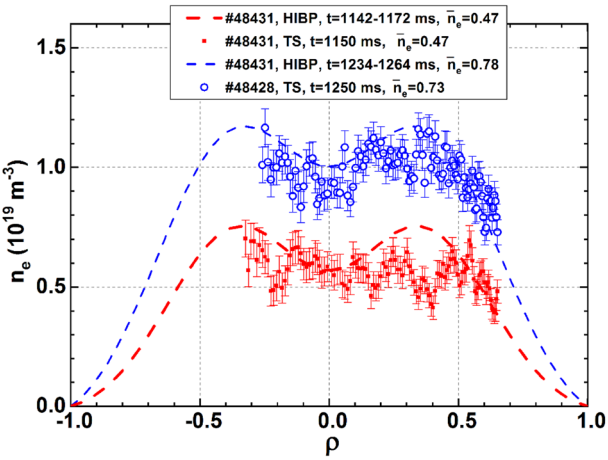

Fig. 5 Plasma density profiles measured by HIBP (dashed lines) compared with Thomson scattering (points) in similar shots with step-wise density evolution; ρ is a normalized plasma minor radius, dimensionless label of the flux surface (Melnikov et al. 2022)

The use of the multi-slit energy analyzer, providing simultaneous measurements in several SVs, extends significantly the HIBP capability in TJ-II. If two sample volumes SV1 and SV2 are placed at the same magnetic surface with poloidal separation, then HIBP with the multi-slit energy analyzer can independently measure several new and unique parameters.

The advanced HIBP II in TJ-II has 5-slits energy analyzer, we obtain five separated SVs, with SV size $\approx$ 1–2 cm placed at the distance $\Delta x_{12} \approx$ 1–2 mm that allows to resolve fluctuations with $k_\theta < 10$ cm^{-1}. HIBP operates in two following modes. The first one is the SV fixed spatial position, used for the detailed study of the AE time evolution. The second one is the SV periodical spatial scan, used for the radial characterization. The SV location can be varied with sawtooth control voltage (in a range of $\pm$5 kV) on the sweeping plates (2) in the primary beamline shown in Fig. 4. We may radially scan from High Field Side, HFS ($\rho = -1$) to Low Field Side, LFS ($\rho = 1$) with scanning time is from 5 to 50 ms, i.e. (20–5) times during the discharge along the so-called detector line. With fast scan, we can observe the slow (diffusive-like) time evolution of mean plasma profiles, while slow scan is focused on the spatial distribution of the turbulence and AEs. Change of the beam energy E_b from shot to shot allows us to vary the detector line in the vertical direction over plasma cross-section. The central detector line is shown as dashed line in Fig. 6 (left). For the 5-slits analyzer, each dash splits to five segments shown in the inset to Fig. 6 (right). Alignment of segments containing the SVs is calculated by a special orbital code. The difference of potentials measured in two poloidally adjacent SV1 and SV2 allows us to obtain the poloidal component of electric field,

$$E_{\mathrm{pol}} = (\varphi_1 - \varphi_2)/\Delta x_{12}. \tag{11}$$

Thus, we can derive the drift plasma radial velocity $\tilde{V}_\mathrm{r}$ in crossed fields E_{pol} and B_t:

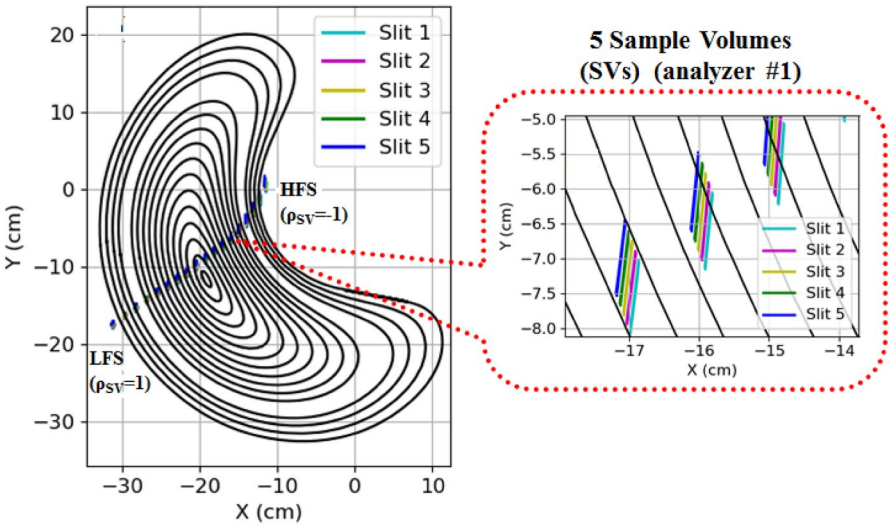

Fig. 6 The TJ-II plasma vertical cross-section at the HIBP location and flux surfaces in the standard magnetic configuration. HIBP II detector line for $E_b = 132$ keV for 5-slits analyzer passes from the low field side (LFS) to the high field side (HFS) near the plasma centre. Inset: poloidal alignment of sample volumes. The origin of coordinates is the axis, around which the plasma column rotates or the centre of the Circular Coil, shown in Fig. 1a. Major axis of the torus has coordinate $x = -150$ cm (Khabanov et al. 2019).

$$\tilde{V}_r = \tilde{V}_{E\times B} \approx \tilde{E}_{\mathrm{pol}}/B_t, \tag{12}$$

and so, the turbulent particle flux

$$\Gamma_{E\times B} = \left\langle \tilde{n}_e \tilde{V}_r \right\rangle. \tag{13}$$

Coupling between the various signals $x(t)$ and $y(t)$, e.g. the density and electric field spectra, is characterised by quadratic coherency coefficient Coh_{xy} and cross-phase θ_{xy}:

$$\mathrm{Coh}_{xy}(f,t) = \gamma^2 = |S_{xy}|^2/|S_{xx}S_{yy}|, \quad 0 < \mathrm{Coh}_{xy} < 1, \tag{14}$$

$$\theta_{\mathrm{xy}}(f,t) = \tan^{-1}\left\{\mathrm{Im}(S_{\mathrm{xy}})/\mathrm{Re}(S_{\mathrm{xy}})\right\}, -\pi < \theta_{\mathrm{xy}} < \pi, \tag{15}$$

where $S_{xx}(f, t)$ is auto-power or power spectral density (PSD) and $S_{xy}(f, t)$ is cross-power Fourier spectrograms. The cross-phase between density fluctuations n_1 and n_2 allows us to measure poloidal wave-vector:

$$k_\theta = \theta_{12}/\Delta x_{12}, \tag{16}$$

velocity of density perturbation propagation or turbulence rotation velocity:

$$V_\theta = 2\pi f \Delta x_{12}/\theta_{12} = 2\pi f/k_\theta, \tag{17}$$

and poloidal mode number:

$$m = Lk_\theta/2\pi, \tag{18}$$

where $L(\rho = \rho_{SV})$ is the circumference of the flux surfaces in the vertical cross-section, neglecting poloidal asymmetry (Eliseev et al. 2012).

Unique capabilities of multichannel HIBP made it the most effective tool to study broadband turbulence and GAM in the core of toroidal devices (Melnikov et al. 2006; Eliseev et al. 2018). Two systems HIBP I and HIBP II, shown in Fig. 3, are shifted about ¼ of torus that allow us to find the long-range toroidal correlations (Sarancha et al. 2022). Details of HIBP hardware and its implementation in TJ-II and also in various fusion devices are summarized in reviews (Melnikov 2016, 2021).

Thus, summarizing the diagnostic description in relation to the AE studies, we underline and compare its advantages and drawbacks. As AE is electromagnetic wave in magnetized plasma, it is characterized by oscillating electric and magnetic fields, accompanied by pressure perturbation. Due to the sensitivity of HIBP to the electric and magnetic potential oscillations along with the density ones with the fine spatial (< 1 cm) and high temporal (< 1 MHz) resolution, it appears to be very instrumental to study AEs even in its basic single-channel version. Its multichannel version provides unique combination of the AE characteristics defined by Eqs. (11)–(18), if the Sample Volumes are properly oriented.

The drawbacks of HIBP are mainly in its technical complexity. The major difficulty is the HIBP operation with high beam energies (E_b and E_d) or accelerating and analyzing voltages, up to 150 keV in the torus hall of TJ-II. Plasma core potential has a range from several dozens of Volts up to a few hundreds of Volts, so it is measured as a minor difference of two large values, which claims the use the high-voltage power supplies with very low level of pulsations ($< 10^{-5}$). The secondary beam current has the typical range of 0.1–100 nA, so the customized low-noise high-bandwidth multichannel transimpedance amplifiers should be developed. Other issues are analyzed in the review (Melnikov 2021).

For tracing the beam through a fusion machine, one should solve the 3D equation of movement for probing particles with many physical, geometry and engineering constrains, so using of HIBP should be planned at the initial phase of machine design to match it with diagnostic ports. Due to such constrains, HIBP in the CHS and LHD stellarators or in the TEXT, JFT-2M, T-10 and JIPPT-IIU tokamaks was capable to probe only limited part of vertical plasma cross-section. In contrast, due to the comfortable location and suitable ports in TJ-II, the probing beam moves along the bean-shaped plasma from LFS to HFS that allows us to probe almost the whole plasma cross-section with reasonably low $E_b < 150$ keV, compared to the similar size machines TEXT, JFT-2M and JIPPT-IIU with $E_b < 500$ keV, TEXT-U with $E_b < 2$ MeV, T-10 with $E_b < 330$ keV, where HIBP has poorer access to plasmas.

4 Alfvén eigenmodes observation

4.1 Time evolution

Plenty of AE modes (Alfvén Zoo) are observed in TJ-II NBI-heated plasmas with frequencies in the range 50–300 kHz, which evolve with plasma density n_e and rotational transform ι (Melnikov et al. 2012, 2010b, 2017b).

Fixed position HIBP measurement shows the separated AEs in the time–frequency domain and the evolution of amplitude and frequency for the observed mode. Example of the measurement at fixed point $\rho = 0.45$ is shown in Fig. 7. The power spectrograms of three HIBP parameters show pronounced AE modes. The mode instantaneous amplitude of the perturbed parameter x in the frequency domain $[f_{\min}, f_{\max}]$ is defined as follows:

$$A_x(t) = \sqrt{\frac{2}{f_{\mathrm{Nyq}}} \int_{f_{\min}}^{f_{\max}} S_{xx}(f,t)\mathrm{d}f}, \tag{19}$$

where f_{Nyq} is the Nyquist frequency.

Figure 7d shows the time evolution of A_φ—amplitudes of the potential perturbation for AEs. Thin lines in (a), (b) and (c) mark the inverse square root Alfvénic dependence of frequency f_{AE} on density:

$$f_{\mathrm{AE}} \propto n_{\mathrm{e}}^{-1/2}(t). \tag{20}$$

Evolution of AEs in discharge, which is started by ECRH ($P_{\mathrm{EC}} = 600$ kW) and followed by counter- and co-NBI (P_{NBI} up to 0.9 MW) is shown in Fig. 8. The

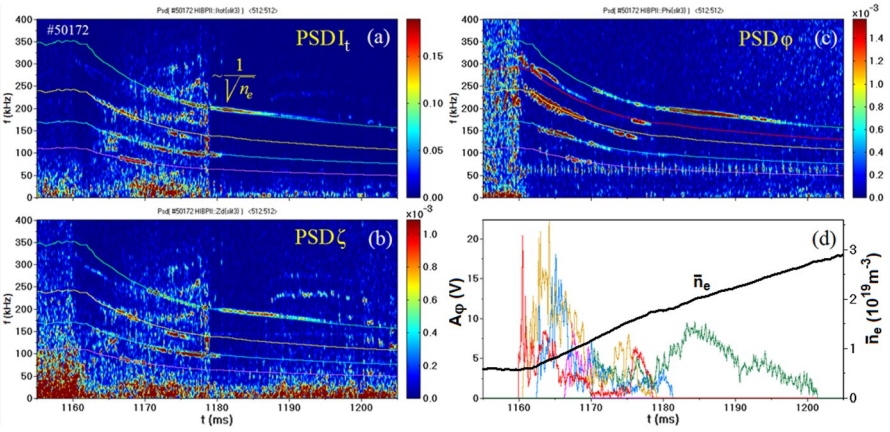

Fig. 7 AE modes evolution in the shot started with ECRH and with rising density due to Co-NBI, $P_{\mathrm{NBI}} = 0.48$ MW, as observed by HIBP in three parameters at $\rho = 0.45$: **a** plasma density (I_t), **b** magnetic potential (ζ), **c** plasma electric potential φ. Thin lines with different colours show Alfvénic dependence on density for several selected modes; **d** line-average density $\bar{n}_e$ and amplitudes of the selected AEs on the plasma potential φ, colour indicates the same modes as in the box (c)

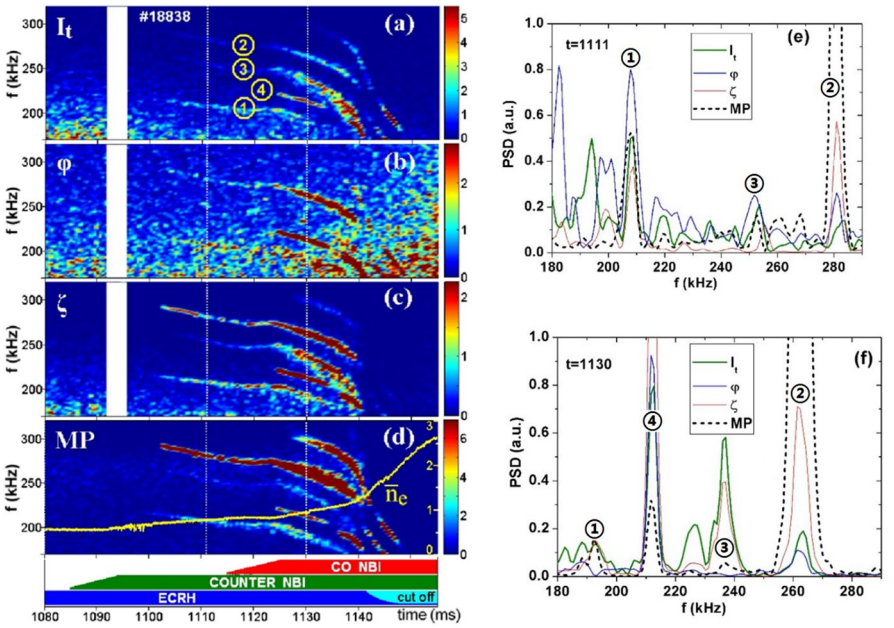

Fig. 8 AE modes evolution in the shot with Co- and Cntr-NBI, $P_{NBI}=0.9$ MW, combined with ECRH ($P_{ECRH}=0.6$ MW, off-axis) observed by three HIBP parameters at $\rho=-0.5$ and magnetic probe (MP). Power spectrograms of HIBP total secondary beam current I_t, i.e. on n_e (**a**); on the plasma potential φ (**b**); on the toroidal secondary beam shift ζ, i.e. on magnetic potential (**c**); and on the MP signal (**d**). The line-averaged density $\overline{n}_e$ is shown by yellow curve in (**d**–**f**) show relative amplitudes of four AEs, marked at (**a**) at two time instants denoted by dotted lines (Melnikov et al. 2010b). Adapted courtesy of IAEA

ECRH phase is characterized by broadband turbulence with $f<200$ kHz, similar to the T-10 tokamak (Melnikov et al. 2018a). After NBI switch-on, the high-frequency AEs are observed by many diagnostics: magnetic Mirnov probes (MP), bolometry, reflectometry, Langmuir probe and HIBP (I_t, φ, ζ). When the density n_e rises, the f_{AE} decreases following the Alfvénic dependence, Eq. (20). Figure 8e, f shows relative amplitudes of four different AEs, designated by numbers in circles at two time instants. Figure 8 shows that each AE mode has an individual 'portrait'–an image in the set of parameters under study. Note that the mode ④ in box (f) is clearly visible in all three HIBP parameters, while the mode ③ in box (e) dominates in density, and the mode ② in boxes (e) and (d) dominates in magnetic signals. Similar to Fig. 7, amplitudes of each mode change in time, and their frequency in the shots with combined ECR + NBI heating follows the inverse square root density dependence, Eq. (20).

4.2 Radial localization of AEs

The radial scanning mode of the HIBP allows us to define the spatial location AEs, as presented in Fig. 9. Figure 9a shows the periodical radial scan of SV, box 9b shows the density fluctuation power spectrogram. Yellow ellipses mark

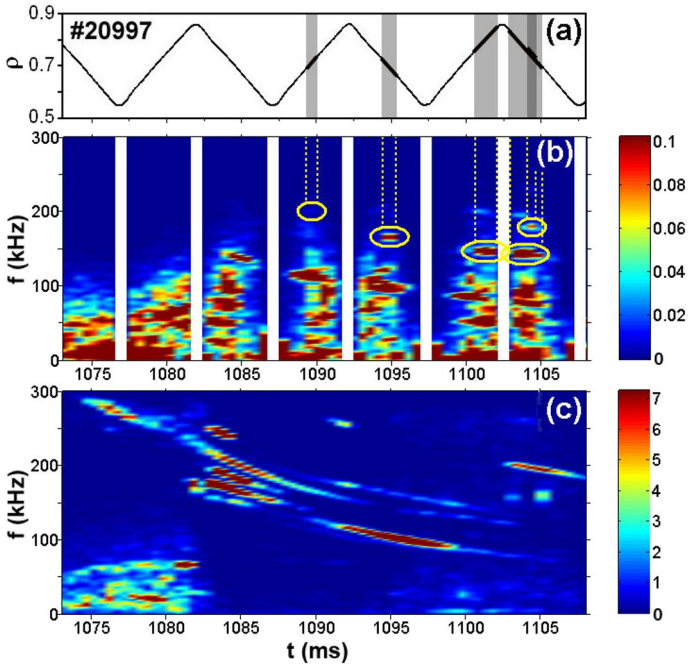

Fig. 9 **a** The radial variation of the sample volume position, scanning time is 5 ms; **b** the HIBP I_t spectrogram indicates the radial location of AEs; **c** magnetic probe spectrogram. Fat lines in **a** designate the areas of AE location. White ribbons in **b** mark HIBP idle periods. Shot #20997, $P_{\text{Co+Cntr-NBI}} = 0.42 + 0.48$ MW, density increases from $\overline{n}_e = 0.66 \times 10^{19}$ m^{-3} to $\overline{n}_e = 3.7 \times 10^{19}$ m^{-3}. Reproduced courtesy of IAEA

quasi-monochromatic high-frequency peaks, corresponding to AEs. Overlapping of time intervals of AEs appearance (grey ribbons) with the radial scan produce their radial localization $0.65 < \rho < 0.85$, marked by fat pieces on the line in box 9(a). The box 9(c) with corresponding spectrogram of the magnetic probe (MP) signal proves that the AEs under study last much longer than they observed by radially moving HIBP SV, so the limits of the mode observation by HIBP are not caused by disappearance of AE due to any reason, but only by the mode radial extent.

In some cases, the reconstruction of the coherence between MP and HIBP data also helps to detect the AE radial extent more clearly. Various modes were observed, there were more peripheral modes and more centrally localized ones. The latter one may be not observed by MP in some cases, this is an issue of the discussed method. For such cases, we use another spatially resolved diagnostics—bolometer array. Such example is shown below in the Fig. 23. The described technique provides the data for the mode radial position in TJ-II plasmas, useful for further analysis and modelling.

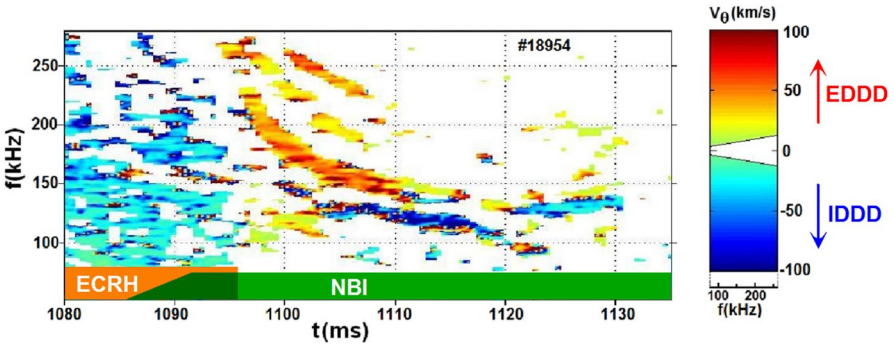

Fig. 10 Spectrogram of poloidal phase velocity of density fluctuations V_θ at $\rho = -0.54$. The only statistically significant values with $\mathrm{Coh}_{n1\ n2} > 0.3$ are shown in colour. The colour bar represents the velocity. The white wedge in colour bar denotes low-velocity interval unresolved due to finite $\Delta x = 1.66$ cm: $|V_\theta| \geq 2\pi f / \left|k_\theta^{\max}\right|$ (Melnikov et al. 2012). Shot starts with ECRH, and followed by NBI accompanied by broadband turbulence suppression and AEs excitation. Broadband turbulence rotates to the ion diamagnetic drift direction (blue colour), while AEs may rotate to ion and electron diamagnetic drift directions (IDDD/EDDD)

4.3 Poloidal rotation dynamics associated with AEs

Multichannel HIBP measurements allow us to reconstruct the 2D frequency–poloidal wave-vector spectrum $S(k_\theta, f)$ with two-point correlation technique (Eliseev et al. 2012). We transform $S(k_\theta, f)$ to $V_\theta(f, t)$ spectrogram and determine the poloidal propagation velocity for AE, using Eqs. (16)–(18). Figure 10 shows an example of such measurement via $V_\theta(f, t)$ spectrogram in the shot with density raise due to NBI fuelling. The positive sign of k_θ and V_θ implies the direction to the electron diamagnetic drift (EDDD). We see that various AEs may rotate in both the electron and ion diamagnetic drift directions (IDDD) with the rotation velocity in a range of dozens km/s. The initial ECRH phase of discharge ($t < 1095$ ms) is characterized by broadband turbulence, which rotates to IDDD. AEs at the start of NBI phase rotate to EDDD. When the density rises, the AE frequencies decrease and the rotation becomes slower or even reverses.

The analysis of local values of k_θ using Eq. (18) may estimate the poloidal mode number m, assuming poloidal symmetry or some level of poloidal asymmetry of the perturbation (Melnikov et al. 2012). Such local estimates typically give reasonably low $m < 6$. The more accurate mode number estimation claims the combine analysis of HIBP and MP array data, planned for the future. Adapted courtesy of IAEA.

4.4 Dynamics of Alfvén modes in experiments with iota evolution

Equations (2)–(3) show that the AE frequency is very sensitive to magnetic configuration or iota change. To study these features at the TJ-II with low magnetic shear, we performed dedicated experiments to check, how the mode frequency depends on the rotational transform, independently varying the currents in coils I_{CC}, I_{HX} and I_{VF} shown in Fig. 1a, and so magnetic fields. First, we dynamically vary the vacuum

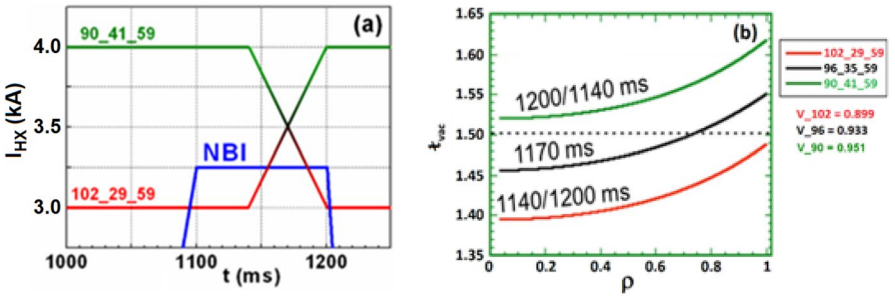

Fig. 11 **a** Time evolution of the vacuum magnetic configuration from the initial one 102_29_59 (red) to the final one 90_41_59 (green) through the intermediate one 96_35_59 (black) and vice-versa; **b** corresponding radial profiles of the ι_{vac} at time instants marked by numbers at the curves during the forward/ backward evolution. Plasma volumes (numbers at the right) in these configurations remain almost unchanged (Melnikov et al. 2004). Reproduced courtesy of IAEA

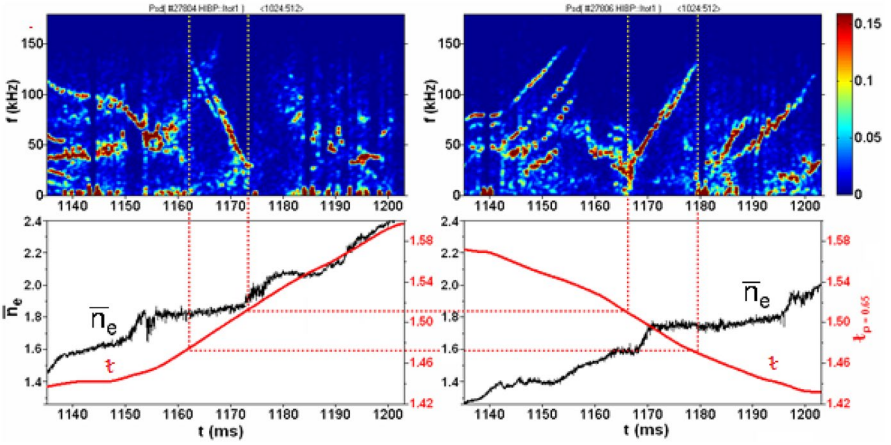

Fig. 12 AE mode time evolution in experiment with ι_{vac} variation ($P_{Co\text{-}NBI}=0.57$ MW). Left figures: ι_{vac} increases, right figures: ι_{vac} decreases; upper figures: the power spectrogram of plasma density, measured by HIBP at adjacent SV positions: $\rho_{SV}=0.7$ in the shot #27804, and $\rho_{SV}=0.5$ in the shot #27806; lower figures: evolution of the line-averaged density ($\times 10^{19}$ m^{-3}) (black lines) and actual ι ($\rho=0.65$) calculated with Eq. (21) (red lines) (Melnikov et al. 2004). Vertical axes for left and right low figures are the same. Vertical dotted lines mark time intervals, in which the similar-looking modes take place; remarkably, they correspond to the same interval of actual iota ramp-up/-down, as marked by horizontal dotted lines

rotational transform in the range: $1.4 < \iota_{vac}(0) < 1.52$. The scenario is presented in Fig. 11. To verify firmly the effect of iota on the AE, we change ι_{vac} up and down symmetrically. Figures 12 and 13 show that during the interval of ι_{vac} change: (i) AEs evolve dramatically and (ii) the changes in plasma current I_{pl} were induced, so magnetic configuration is not determined by only ι_{vac} anymore. For the actual iota, determining magnetic configuration, and including plasma current contribution, we propose a simple linear model (Melnikov et al. 2004):

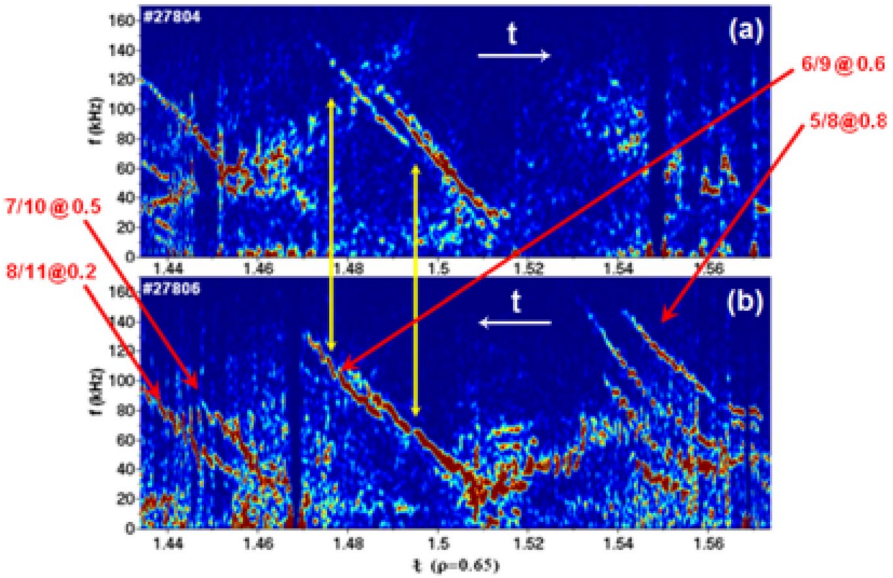

Fig. 13 Power spectrograms of plasma density from Fig. 12, replotted as a function of the actual ι by Eq. (21) instead of time. Note that in box (b) a time pass oppositely to ι. The vertical yellow arrows mark the same modes, observed during the ι_{vac} ramp-up and ramp-down. Red arrows and numbers mark modelling values of m/n at ρ_{AE} (Melnikov et al. 2004). Reproduced courtesy of IAEA

$$\iota(\rho_{AE}, t) = \iota_{vac}(\rho_{AE}, t) + C(\rho_{AE}) I_{pl}(t) + \delta\iota. \tag{21}$$

The $C(\rho)$ profile is a time-permanent fit for the ι profiles, obtained by the equilibrium calculations for $|I_{pl}| < 8.5$ kA (López-Bruna et al. 2004). The output parameters of the model: the mode numbers m, n and its origination radius ρ_{AE} are chosen as the best fit for the time traces of the mode frequency $f_{AE}(t)$ along the total time interval of the mode existence. The term $\delta\iota$ is the iota correction constant, independent of ρ and t. It compensates the uncertainty in the current profile. Typically it's value has an order of $(\iota_{vac}(a) - \iota_{vac}(0))/N$, where $N \sim 3$–4. Red numbers in Fig. 13 mark modelling results: ratio of m/n at ρ_{AE}.

Mode frequency evolution at the constant ι_{vac} highlights the role of plasma current in AE evolution. The strongest effect was obtained with I_{VF} modulation (Fig. 14). We see that I_{VF} decrease in 10% induces the I_{pl} decrease up to 5 kA and the drastic change of AE frequency from 35 to 250 kHz. The vacuum iota does not change, but I_{VF} induces plasma current I_{pl} that modifies the iota profile. Figure shows that the maximum of f_{AE} is synchronized with the minimum of I_{pl}, while both are delayed by 2 ms from I_{VF} (vertical dotted lines in Fig. 14a, b). Minor contribution of $\delta\iota$ term in the model is shown in Fig. 14b.

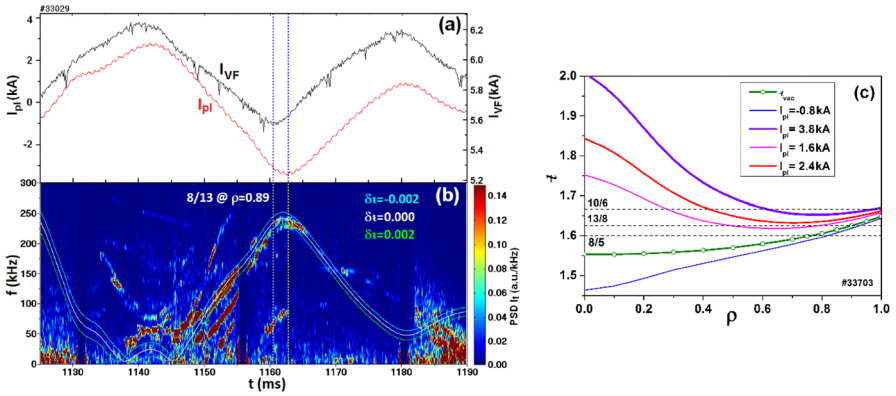

Fig. 14 Shot #33029 ($P_{\text{Cntr-NBI}}=0.57$ MW) with AE evolution due to sawtooth changes of vertical field VF: **a** time traces of vertical field I_{VF} and plasma I_{pl} currents; **b** density PSD measured by HIBP at $\rho_{\text{SV}}=0.46$ and the modelling results by Eq. (21) for the chosen mode $m/n=8/13$, and the sensitivity to the ι fitting, $\delta\iota = \pm 2\times 10^{-3}$; **c** rotational transform with different plasma currents I_{pl}. Several relevant rational resonances are marked by dashes (Melnikov et al. 2004). Reproduced courtesy of IAEA

4.5 Constancy of the AE radial position respect to the iota and density variation

AE frequency shows significant evolution with spontaneous and forced iota variation, as shown in the previous sections. It also evolves with density consistent to the Alfvén law. It is important to learn, whether the mode radial position changes with iota or density. Figure 15 shows the spectrogram of density fluctuation during the periodical radial scans from $\rho=-1$ to $\rho=+1$ along with the beam current I_t, line-averaged density $\overline{n}_{\text{e}}$ and the plasma current I_{pl}. We see that while I_{pl} changes in a range of $0<I_{\text{pl}}<-2.76$ kA, the plasma density evolves in a factor of ~2, the rotational transform modelled with Eq. (21) at $\rho=0.7$ changes in range of $1.529<\iota<1.571$, and the AE frequency changes in a factor of >2 (from 230 to 120 kHz), however, the mode localization does not change, as shown in box (e) (Melnikov et al. 2004). These observations were supported by the measurements in the fixed SV position.

The present analysis shows that the AEs frequencies are very sensitive to the iota: even a small iota variation causes the change of f_{AE} up to the factor of 7, contrary, the mode radial position remains the same. The analysis of AEs, observed in TJ-II since the first identification in 2010 (Melnikov et al. 2010a) up to now, shows that the model for f_{AE} with Eqs. (1, 2, 3, 21) describes all observed modes within the experimental accuracy without exceptions (Melnikov et al. 2004, 2016b, 2017b, 2018a, b; Melnikov 2019, 2021; Weisen et al. 2011; Eliseev et al. 2021). Note that the model assumes the constancy of the ρ_{AE}, which consists with the observations. The model is verified for relatively high mode frequency. Dynamics of f_{AE} near its low limit is considered in the next section.

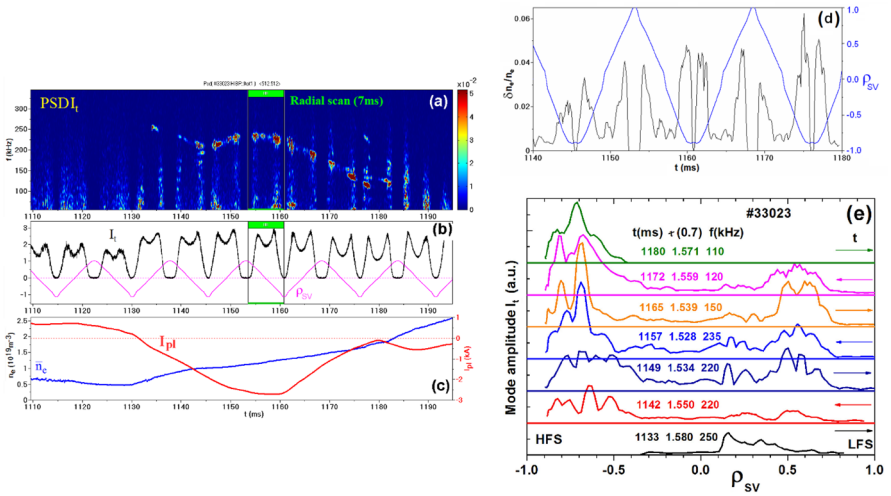

Fig. 15 Mode location study with HIBP radial scan in shot with Cntr-NBI ($P_{NBI}=0.57$ MW) and saw-tooth-like variation of ɾ and current I_{pl}. **a** Spectrogram of total beam current I_t (density) fluctuations; **b** signal of I_t and SV radial position ρ_{SV}; **c** evolution of plasma current I_{pl} and line-average density $\overline{n}_e$; **d** density fluctuations $\delta n_e/n_e$ and SV radial position ρ_{SV}; **e** Time evolution of the radial profiles of density perturbation caused by AE. Mode location is poloidally symmetric (LFS-HFS) and permanent in time during ɾ evolution (Melnikov et al. 2004). Reproduced courtesy of IAEA

5 Observation of non-zero limit for AE frequency

5.1 Experiment and analytical model

We show in previous sections that f_{AE} strongly depends on magnetic configuration and may vary in several times during one shot. As mentioned in Introduction, GAMs and AEs have common dispersion relation. Some theories and gyrokinetic modelling predict that energetic particles may excite both AEs and GAMs, and thus stabilize the ion temperature gradient (ITG) driven turbulence (Siena et al. 2019b). We have performed dedicated experiments to study AE frequency dynamics near its lower limit of and to seek predicted relation between AEs and GAMs (Eliseev et al. 2021). In contrast to the earlier studies in the configurations with high magnetic shear at the DIII-D tokamak (Zeeland et al. 2016) and LHD stellarator (Toi et al. 2010), we focused on the low magnetic shear configurations in TJ-II. Figure 16 presents the experimental results. Modulation of the vertical coil current I_{VF} induces modulation of plasma current I_{pl}. Alfvén modes evolution is observed by the magnetic probes (MP), bolometers (Bol) and by HIBP with total beam current I_t, proportional to the density, and plasma potential φ. Thin lines in Fig. 16b correspond to best fitting from the f_{AE} model with Eqs. (1)–(3), (21), which neglects the GAM contribution in the dispersion relation. Figure clearly shows existence of the non-zero lower limit for f_{AE}. For its analysis, we extended the dispersion relation (Breizman et al. 2005):

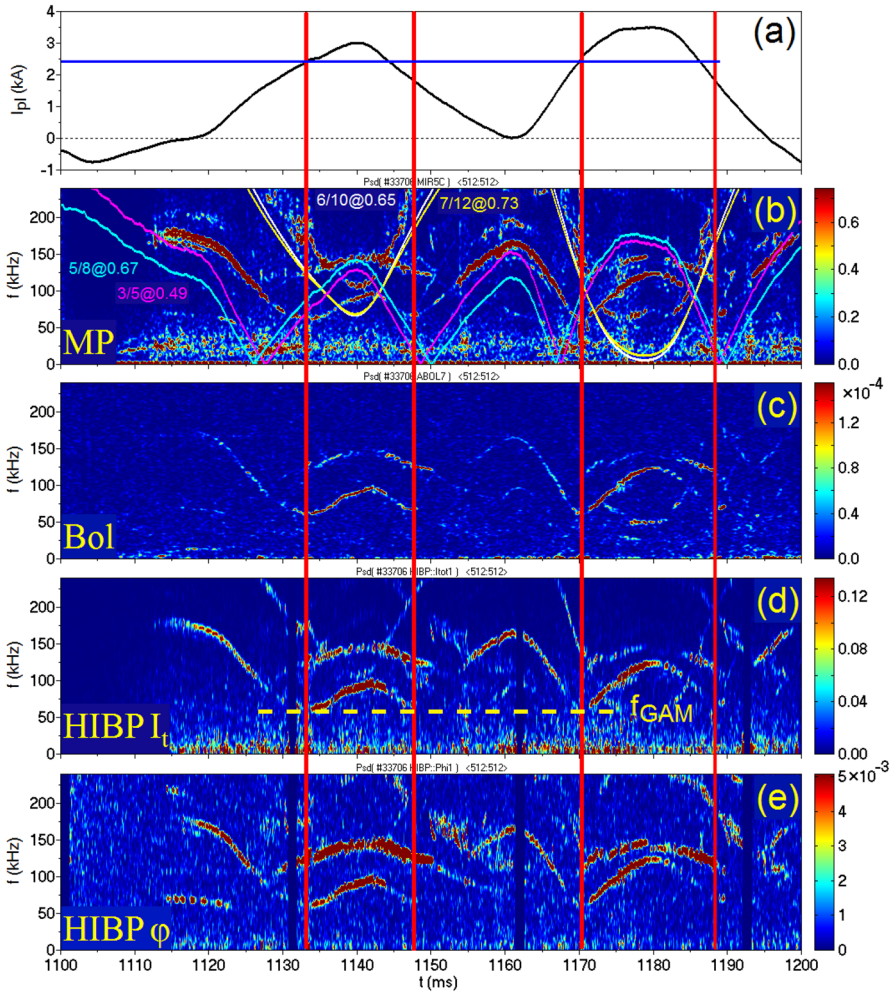

Fig. 16 Evidence of the lower limit of AE frequency. Shot #33706, $P_{\text{Co-NBI}} = 0.56$ MW, sawtooth-like variation of vertical field. **a** Variation of plasma current I_{pl}; **b** PSD signal of magnetic probe and best fittings with model Eqs. (1, 2, 3, 21); **c** PSD of plasma emissivity measured by bolometer at $\rho = 0.1$; **d** PSD of total beam current at $\rho = 0.36$; **e** PSD of plasma potential. Dashed line marks the minima of f_{AE}, consistent with GAM frequency f_{GAM} calculated with Eq. (23); Vertical lines mark local minima of AE frequency, which are coupled with the specific value of $I_{\text{pl}} = 2.5$ kA (blue line in (**a**)), but not with extrema in plasma current or iota. The results of the modelling with Eqs. (21)–(23) describes observations with $m, n, \rho, f_{\text{GAM}}$ fitting parameters, while $f_{\text{GAM}} = 60$ kHz agrees to (23) with measured T_e ($\rho = 0.2$).

$$f_{\text{AE}}^2(\rho, t) = \left(\frac{1}{2\pi R} |m\iota(\rho, t) - n| V_A \right)^2 + f_{\text{GAM}}^2, \tag{22}$$

where ι is defined by Eq. (21) and f_{GAM} is determined as (Winsor et al. 1968):

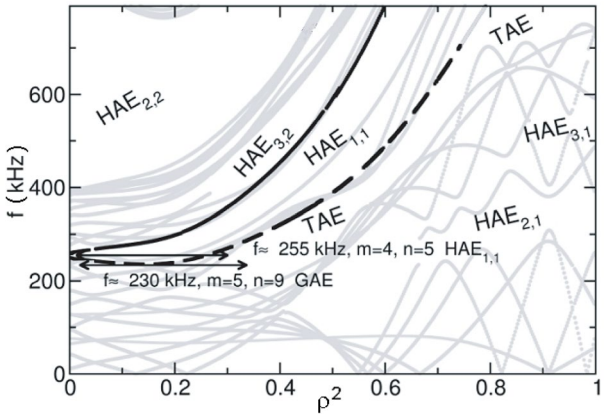

Fig. 17 Alfvén continuum for the shot #18838 presented in Fig. 8 at $t = 1140$ ms, with multiple gaps for several modes: GAE, TAE and various families of $HAE_{n,m}$ calculated by CONTY code (Melnikov et al. 2010c)

$$f_{\mathrm{GAM}}(\rho) = \frac{1}{2\pi R}\sqrt{\frac{\left(T_e(\rho) + \frac{7}{4}T_i(\rho)\right)}{m_i}\left(2 + \iota^2(\rho)\right)}. \tag{23}$$

5.2 Comparison with numerical simulations

MHD modelling allows us to identify the type of Alfvén modes in TJ-II as Helicity-induced Alfvén eigenmodes (HAEs) (Nakajima et al. 1992), Global Alfvén eigenmodes (GAEs) (Appert et al. 1147) and Reversed Shear Alfvén Modes (RSAEs) (Zeeland et al. 2016). The set of AE families, calculated with the ideal MHD code CONTY for the shot #18838 shown in Fig. 8, is presented in Fig. 17 (Melnikov et al. 2010c). Calculations show that several gaps in Alfvén continuum may exist, where various types of AEs driven by fast particles may be excited in the frequency range, where several coexisting modes were observed.

Figures 18 and 19 present the mode identification with AE3D model for the shot #18838 in terms of Alfvén mode numbers and spatial structure calculated with the AE3D code (Spong et al. 2010), while the Alfvén continuum was obtained with the MHD code STELLGAP (Spong et al. 2003). The odd toroidal modes from $n = 1$ up to $n = 17$ were used to represent eigenfunctions with poloidal number m from 10 to 30. Figure 18a shows the density cross-phase θ_{nn} spectrogram for oscillations observed in two poloidally shifted SVs, while box (b) shows the θ_{nn} histogram. The box (c) presents the calculated radial structure of the observed mode with the frequency 241.1 kHz. Modelled mode is dominated by the coupling between $n/m = 1/1$ and $n/m = 7/4$ components. The experimental values for this particular mode are $m = 4.4 \pm 2.2$, so the estimated $n = m\iota = 6.6 \pm 3.2$. The modelling values

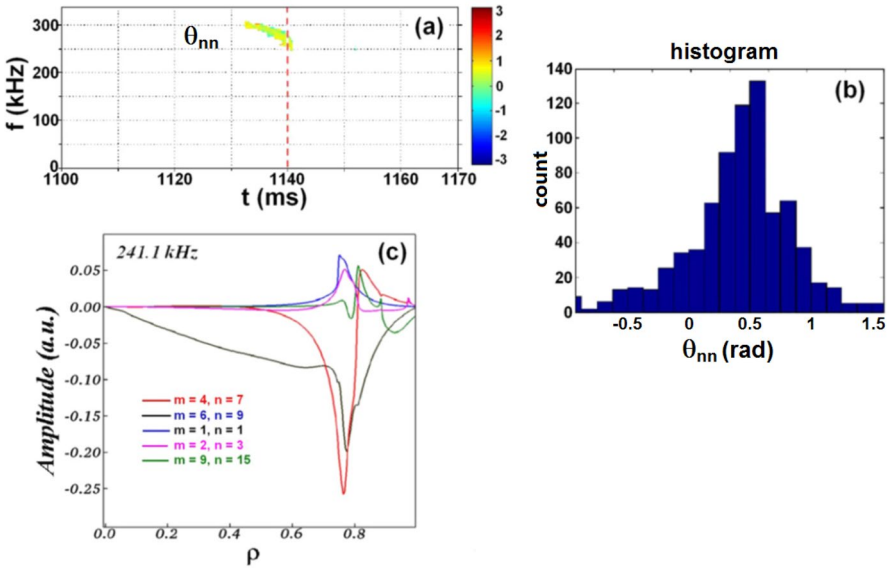

Fig. 18 Mode identification with AE3D model in shot #18838 presented in Fig. 8: **a** power spectrogram of the cross-phase θ_{nn} between n_e oscillations, observed in two poloidally shifted SVs, the only branch under study is presented (colour bar is in radians), **b** the histogram of θ_{nn} for the presented branch; $\theta/\pi = 0.148 \pm 0.07$, $m = 4.4 \pm 2.2$, $n = 6.6 \pm 3.2$; **c** the calculated HAE structure on plasma potential at 241.1 kHz (Melnikov et al. 2012). Reproduced courtesy of IAEA

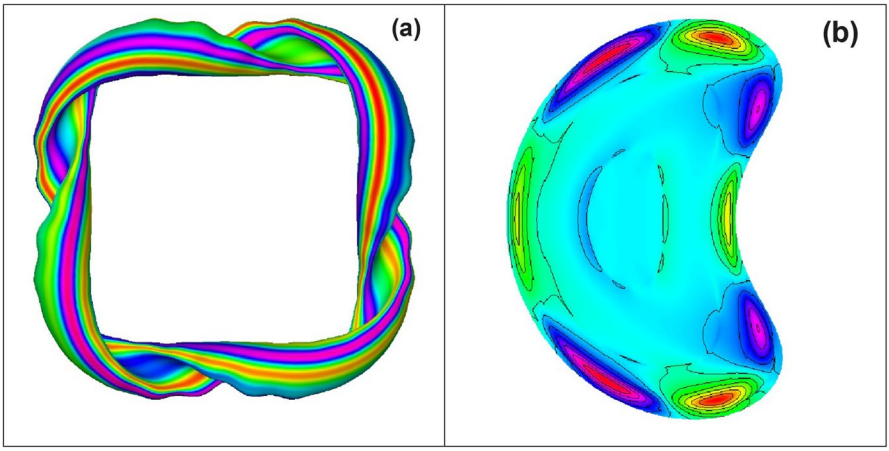

Fig. 19 #18838: Top view (**a**) and vertical cut (**b**) of the 3D mode structure for identified HAE with dominating component $n/m = 7/4$ (Melnikov et al. 2012). Reproduced courtesy of IAEA

for $n/m = 7/4$ agree with the measured ones within the experimental accuracy. These values are in agreement with the low-order rational values expected from the ι profile (similar to the one shown in Fig. 14c). Finally, the experimentally observed

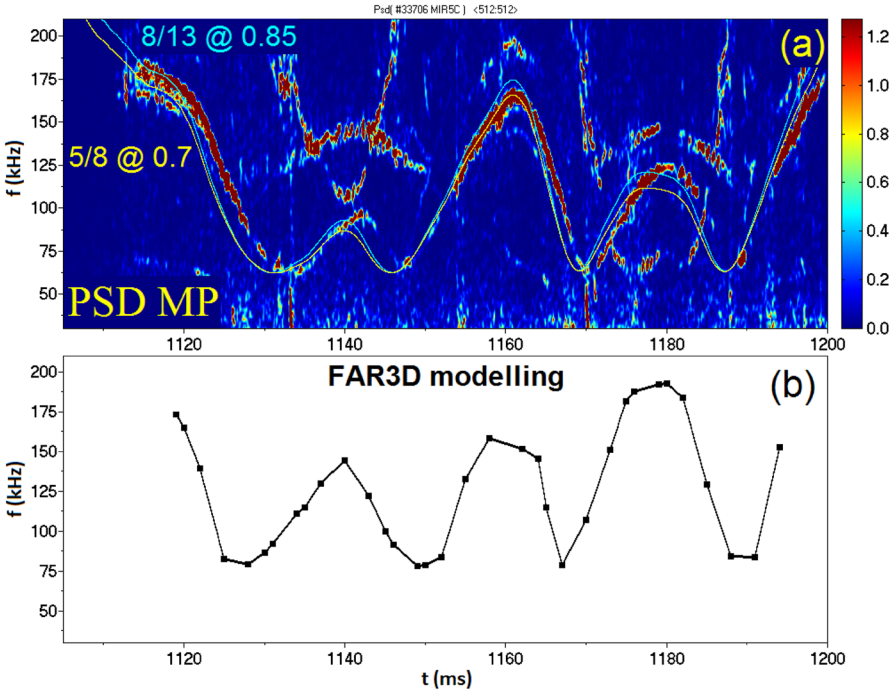

Fig. 20 AE dynamics in plasma scenario with Co-NBI and sawtooth I_{VF} and I_{pl} variation shown in Fig. 16. **a** PSD of magnetic fluctuations measured by magnetic probe and two analytical fits by Eqs. (21)–(23) for $f_{GAM}=62$ kHz: 8/13 @ $\rho=0.85$ in blue and 5/8 @ $\rho=0.7$ in yellow; **b** Simulation of the AELM frequency by the FAR3D code gives 5/8 mode reproducing the mode frequency sweeping (Eliseev et al. 2021)

$n/m = 7/4$ mode can be identified as HAE (Nakajima et al. 1992). Figure 19 presents 3D structure of the identified mode.

The structure of Alfvén continuum and gaps for the shot #33706 with iota variation described in Sect. 5.1 was calculated with the STELLGAP, and the time evolution of the mode frequency was calculated with the gyro-fluid FAR3D code (Spong et al. 2021). Comparison of experimental spectrogram with FAR3D simulation is presented in Fig. 20. We see that the simple analytical estimation (21)–(23) for f_{AE} with the determined mode numbers m, n and location reproduces the observations over the whole time of the mode existence. Note that it also holds for the time instants, when ι is equal to value $\iota = n/m$ at the mode location due to the plasma current I_{pl}. In these instants, the parallel wave-vector $k_{||}$ (Eq. 3) vanishes, and AE frequency has a minimum close to f_{GAM} (Eq. 22). Simulations with the codes STELLGAP and FAR3D reproduces the AE frequency variation caused by I_{pl} changes and the mode numbers of the analytical model (21)–(23). Note that location of the simulated eigenfunction is placed at the outer edge of the observed mode.

FAR3D is also instrumental to simulate the mode radial location. Figure 21 shows the amplitude of the mode $n/m=7/4$ calculated by FAR3D and measured by

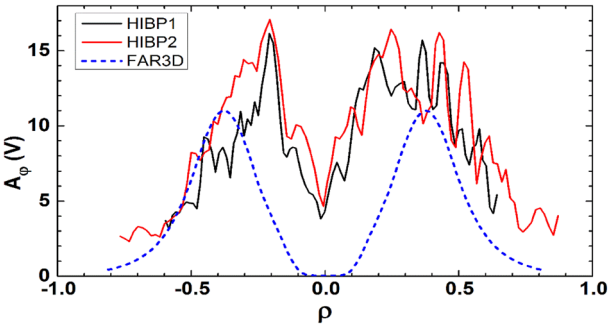

Fig. 21 Amplitude of the potential perturbations at the frequency 100 kHz (solid lines), observed by dual HIBP, and HAE mode $n/m = 7/4$ simulated by FAR3D (blue dashed line). The steady-state phase of shot #44257 with Co-NBI ($P_{\mathrm{NBI}}=0.5$ MW) combined with ECRH/ECCD ($P_{\mathrm{EC}}=480$ kW) at $\overline{n}_e \sim 0.7\times10^{19}$ m^{-3} (Cappa et al. 2021). Adapted courtesy of IAEA

dual HIBP system in the regime with combined NBI and ECRH/ECCD. The mode is observed at the steady-state phase of the shot at the frequency 100 kHz. Note that the changes of magnetic configuration by small plasma current ($I_{\mathrm{pl}}<1$ kA) affected by ECCD, strongly affects the spectrum of AE, as predicted by FAR3D. In spite of uncertainties, owing to estimations of rotational transform, the code predictions are in reasonable agreement with the observation in the mode frequency, radial location and the absolute value of the plasma potential perturbation (Cappa et al. 2021).

6 AE-induced radial particle flux

As we mention in Sect. 3, HIBP with the multi-slit analyzer is sensitive to the turbulent particle flux $\Gamma_{E\times B}$, Eq. (13). The frequency-resolved data allow us to reconstruct the flux spectral function as (Eliseev et al. 2018):

$$\Gamma_{E\times B}(f,t) = \frac{1}{B_{\mathrm{t}}}\mathrm{Re}(S_{n_e E_\theta}(f,t)), \tag{25}$$

where Re means the real part of the cross-power spectra of plasma density and poloidal electric field E_θ. Direction of the instant flux contribution at each frequency depends on the cross-phase θ between fluctuations of n_e and radial velocity or E_θ (Eq. 25). Figure 22 shows the frequency-resolved flux function in the shot with NBI-heating from Fig. 8. It shows quite pronounced quasi-monochromatic peaks of AEs contrasting to the intermittent character of the broadband turbulence flux. Most of the AEs contribute to the outward or positive flux shown in red (average $\theta\sim-3\pi/4$), however, some modes generate the inward or negative flux shown in blue ($\theta\sim0$), and some AEs did not generate any flux at all ($\theta\sim-\pi/2$).

Figure 22 shows that the cross-phase between n_e and E_{pol} fluctuations excited by AE is not universal one, forming auxiliary losses through the outward $E\times B$ particle flux, as one may expect from any kind of instability. Contrary, being an individual

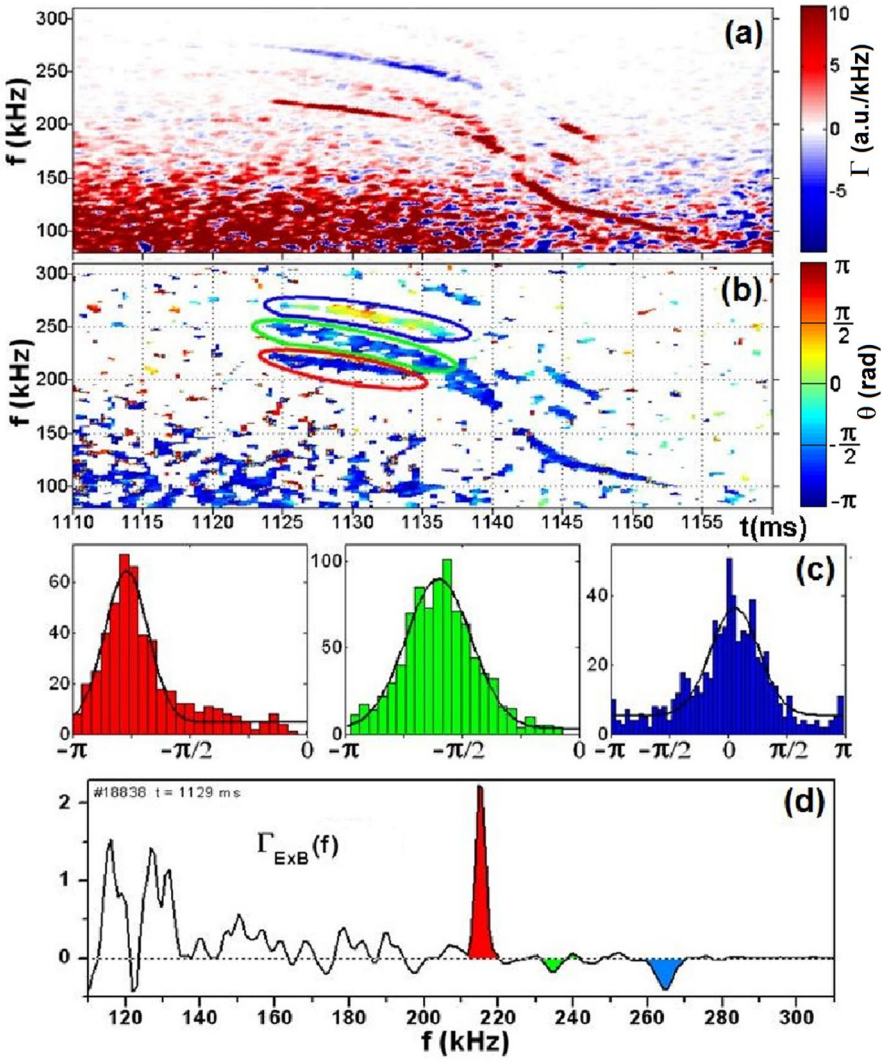

Fig. 22 **a** Time evolution of frequency-resolved turbulent particle flux for shot from Fig. 8; **b** Cross-phase between n_e and E_{pol} fluctuations. The colour ovals mark chosen AEs; **c** the cross-phase histograms for each AE is painted by colour, indicating direction of flux: left box–outward (red), central box–zero flux (green), right box–inward (blue); **d** power spectrum of the turbulent particle flux with three painted frequency peaks designate chosen AEs (Melnikov et al. 2012)

characteristic of AE, the flux can be directed outwards, inwards, or the mode can generate zero flux. Figure 22d shows that the AE-induced turbulent particle flux may exceed the one driven by the broadband turbulence at the same frequency range up to a factor of 10, so AEs may contribute significantly to the total particle flux. (Melnikov et al. 2012). Reproduced courtesy of IAEA.

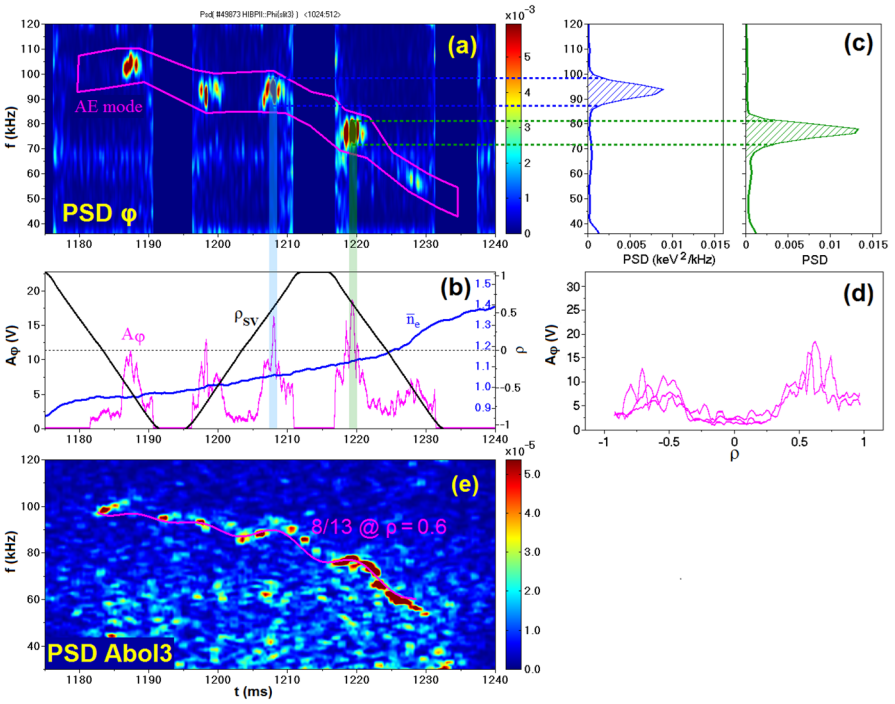

Fig. 23 HIBP measurements of the AE spatial structure in shot with rising density ($P_{\text{Co-NBI}} = 0.51$ MW). **a** PSD of plasma potential fluctuations in HIBP scanning mode. The single AE is enclosed by magenta polygon; **b** temporal evolution of HIBP SV minor radius ρ_{SV} (black), AE amplitude A_φ (t) calculated with Eq. (19) (magenta) and line-averaged density $\bar{n}_e$ (blue); **c** PSD of AE in two time instants; **d** permanent ballooning radial profiles of the AE amplitude $A_\varphi(\rho)$ by several radial scans; **e** PSD of bolometer signal along the chord at $\rho = 0.6$. Magenta line shows the modelling results with Eqs. (1, 2, 3, 21) (Melnikov et al. 2022)

7 2D distribution of the AE amplitude

Upgrading of HIBP diagnostics allows us to observe the full radial interval and considerable part of the vertical cross-section in a series of reproducible shots (Melnikov et al. 2017b; Sharma et al. 2020). Figure 23a shows power spectrogram of plasma potential, obtained in HIBP scanning mode, with single pronounced AE, evolving in time in line with the density and ⊬ evolution. AE under study is highlighted by magenta line. Box (b) shows AE amplitude time evolution obtained by HIBP scan. Box (c) shows the frequency structure of chosen AE in two time instants, and box (d) shows that radial profiles of AE amplitude during these serial radial scans is almost permanent. Bolometer data, box (e), confirms that we see the single AE. It is also consistent with the modelling results by Eqs. (1, 2, 3, 21).

Figure 24 presents the 2D map of the AE, which was obtained in the series of reproducible shots by taking together a set of radial scans with various E_b. Figure shows that AE mode induced potential perturbation is distributed along the flux

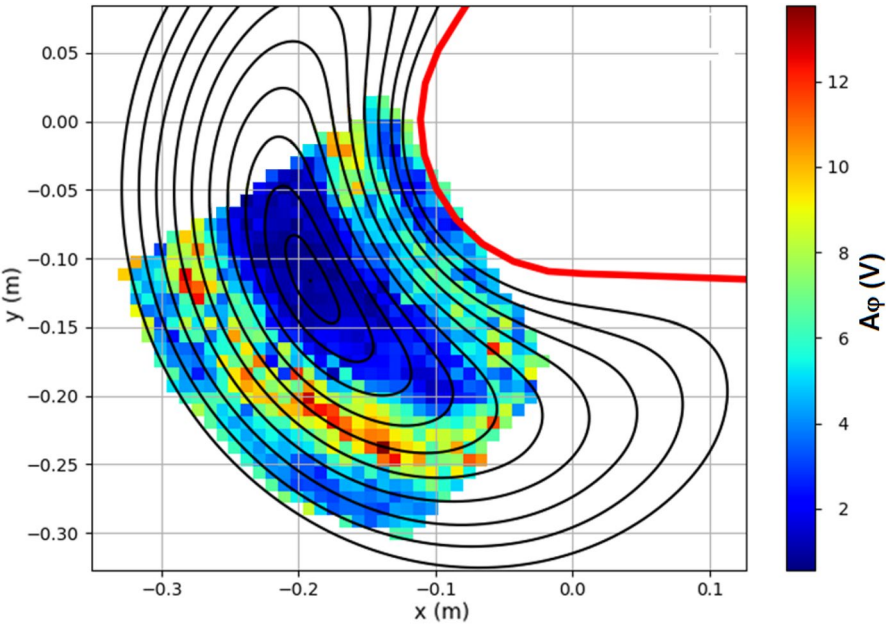

Fig. 24. 2D map of AE in NBI plasma of TJ-II ($P_{\text{Cntr-NBI}}=0.51$ MW). Ballooning structure of AE amplitude in plasma potential (colour bar) with maximum at LFS, $\rho=0.6$, measured shot-by-shot by HIBP beam energy scan ($E_b=90$–150 keV). Red line is a part of vacuum chamber (Melnikov et al. 2022)

surfaces. The perturbation amplitude is not poloidally uniform, but has a ballooning character on the flux surface, dominating on LFS by a factor of 1.5 with respect to HFS. Such ballooning distribution is typical for AE in TJ-II.

8 Chirping modes

Now we discuss features of chirping Alfvén modes. Chirping modes are sequence of separated bursts with fast frequency variation up or down in each individual burst. In TJ-II, they typically observed in low-density NBI + ECRH plasmas, so ECRH may be a sufficient (but not necessary) condition for existing of the chirping AEs, because these modes sometimes appear in NBI-only plasmas. Figure 25 shows the transition of AE from chirping to steady-frequency form observed in NBI + ECRH plasma after ECRH turn-off (Melnikov et al. 2016b). In shots with iota variation, it was shown an existence of ι windows favorable for chirping and quasi-steady-frequency form of AE and smooth transition between them. Examples of such shots are presented in Fig. 26.

In two shots with similar density, heating power and ι_{vac} range, ι_{vac} has opposed evolution. Both shots demonstrate the sequence: chirping–steady mode–chirping, designates by yellow squares in boxes (a) and (b). Details of transformation are clearly seen in boxes (c) and (d). The double structure of the chirping modes with a hook-like pattern is transformed to a double steady-frequency form and then back to

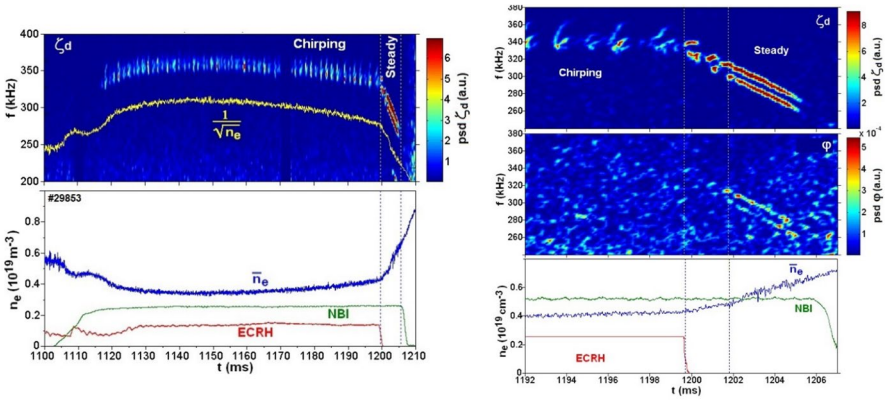

Fig. 25 Transformation of AE from chirping to steady-frequency form after ECRH switch-off. Left: PSD of magnetic potential (ζ_d) at $\rho = -0.6$, plasma density n_e, ECR and NBI-heating power ($P_{EC} = 0.25$ MW, $P_{Co\text{-}NBI} = 0.56$ MW). Right: zoom of left column with added middle box—PSD of potential φ perturbation. Transition period ~ 2 ms between ECRH switch-off and steady-frequency AE formation is seen (Melnikov et al. 2016b). Reproduced courtesy of IAEA

a double chirping form. Note the smooth evolution of the AE mean frequency along this transformation chirping-steady-chirping and back. Favorable iota windows are marked by thick lines and rectangles in box (e). We redraw boxes (a) and (b) as functions of iota and more clearly show the borders of iota windows favorable to steady-state and chirping modes (red dash lines in boxes (g) and (h)).

Chirping modes demonstrate a great variability. Figure 27 presents various types of the frequency evolution: convex-up, convex-down, hook, *i*-type, sickle, and linear (Melnikov et al. 2018b). The hook type was observed in some other fusion devices, e.g. in the JET tokamak (Berk et al. 2006).

Chirping modes may evolve in time with minor changes of iota or plasma current. Slow in time and narrow in space radial scan of HIBP allows us to estimate the radial width of each burst and the rate of its radial propagation. Example of such observations are shown in Fig. 28. Some of the AE chirping mode have permanent localization as the most of observed steady AE modes. However, there are examples of significant change in localization of chirping mode during its burst, boxes (a–c). Box (d) shows that the convex-down type of AE in HIBP signals depends on ρ: if $|\rho|$ larger, the burst starts later and has higher initial frequency f^* at ρ^*. The burst originates at $|\rho| \leq 0.4$ and then expands outward up to $|\rho| = 0.7$ with frequency raise, which corresponds to the Alfvén law, Eq. (20), on the density: during the radial propagation of burst, the density falls down in a factor of 2, and the frequency correspondingly increases in a factor of $\sqrt{2}$. The average radial velocity of the burst propagation is about 70 m/s. The box (d) can also be used in another way: for given frequency f^* one may determine the radial interval of the burst propagation from $|\rho^*|$ till the maximal value for the mode under study, $|\rho^*| = 0.7$.

Another example of transformation from steady to chirping AEs and back is shown in Fig. 29 (Melnikov et al. 2018a). In pure-NBI plasma the only steady-frequency AE appears, but after switch-on of one additional gyrotron with

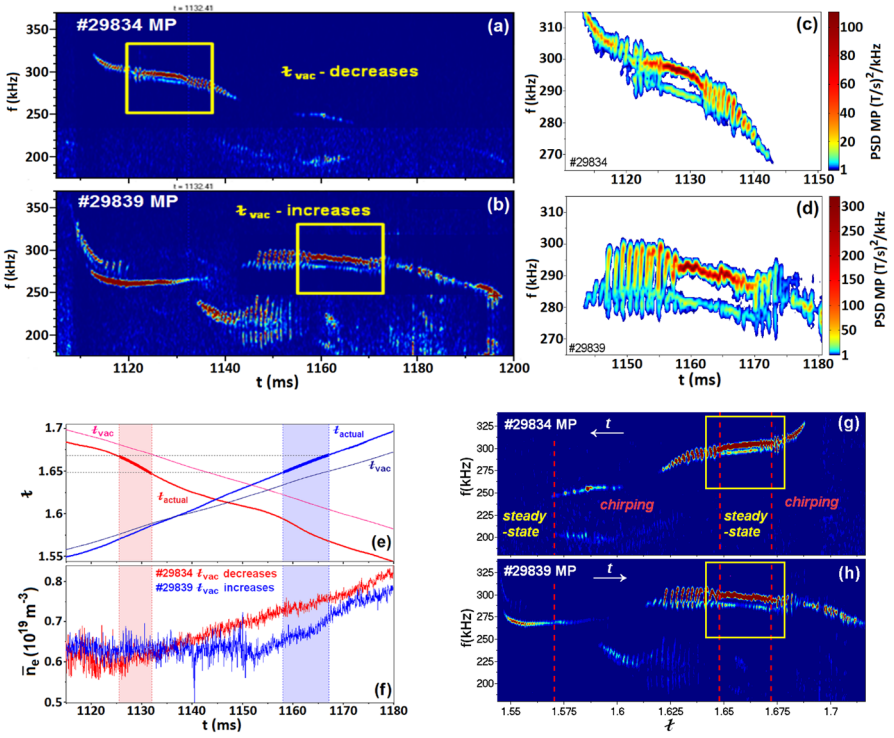

Fig. 26 Transformation of AE from chirping to steady-frequency form with forced ι_{vac} variation. Shots with $P_{\text{Co-NBI}} = 0.56$ MW. Magnetic spectrograms for shots with ι_{vac} decrease (**a**) and ι_{vac} increase (**b**); (**c**) and (**d**) show fine details of the mode transformation, they are zooms of (**a**) and (**b**); (**e**) time evolution of ι_{vac}, thick parts of curves show evolution of actual ι; (**f**) presents time evolution of densities; (**g**) and (**h**) are redrawn (**a**) and (**b**) as function of actual ι. Vertical dashed lines distinguish actual ι windows, favorable for steady-frequency and chirping modes Actual ι was calculated with Eq. (21) at $\rho = 0.55$ (Melnikov et al. 2016a). Reproduced courtesy of IAEA

$P_{\text{ECRH2}} = 300$ kW, AE transforms from steady to chirping form with approximately the same amplitude. Surprisingly, the further increase ECRH power up to 600 kW (switch-on the second gyrotron) causes the mitigation of AE. It is clearly seen on the amplitude of magnetic fluctuations that decreases in a factor of 5, box (e). Electrostatic potential φ fluctuations are also suppressed, their amplitude decreases in a factor of 1.5, box (c). Note that suppression of AE is accompanied by the density pump-out and excitation of the broadband turbulence, clearly seen in boxes (a) and (d).

Note that various mechanisms of AEs stabilization by ECRH/ECCD are considered, of which the main ones are: a local T_e increase accompanied by the n_e decrease due to the pump-out, leading to a change in the pressure gradient of the main plasma and slowing-down rate of fast particles, a change in the pressure gradient of energetic particles, which are the source of AE excitation and the electron Landau damping (Garcia-Munoz et al. 2019). One of the most straightforward one is the iota

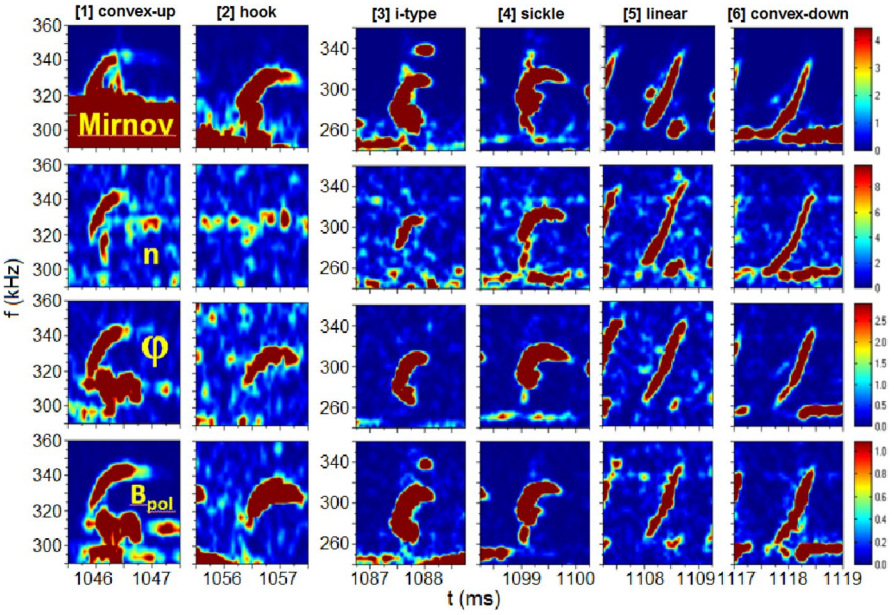

Fig. 27 Various patterns of chirping AE observed in a single shot #39116 with rising density $\overline{n}_e \sim 0.3$–0.5×10^{19} m^{-3}, $P_{\text{Co-NBI}} = 0.58$ MW, $P_{\text{Cntr-NBI}} = 0.42$ MW) (Melnikov et al. 2018b). Reproduced courtesy of IAEA

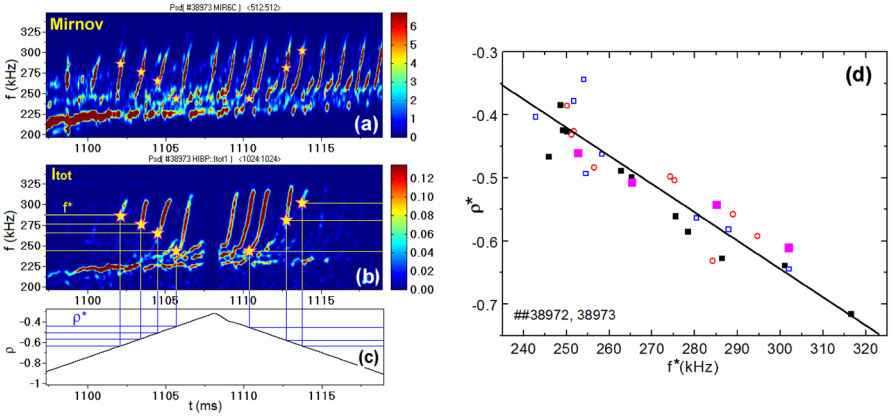

Fig. 28 Observation of outward expanding convex-down pattern of chirping-up AE. Shot #38973, $P_{\text{Cntr-NBI}} = 0.43$ MW, $\overline{n}_e \approx 0.7 \times 10^{19}$ m^{-3}. **a** Magnetic power spectrogram by MP shows the full picture of burst irrespectable on locality; **b** local measurements of density fluctuations power spectrogram by HIBP I_t shows the part of burst locally observed; **c** radial scan of HIBP Sample Volume in terms of $\rho(t)$; five-end stars in (**b**) and (**c**) mark initial frequency f^* and radial position ρ^* of each burst; (**d**) outer bound of chirping-up AE modes as a function of initial burst frequency, collected data for plasma density and potential PSDs (Melnikov et al. 2018b). Reproduced courtesy of IAEA

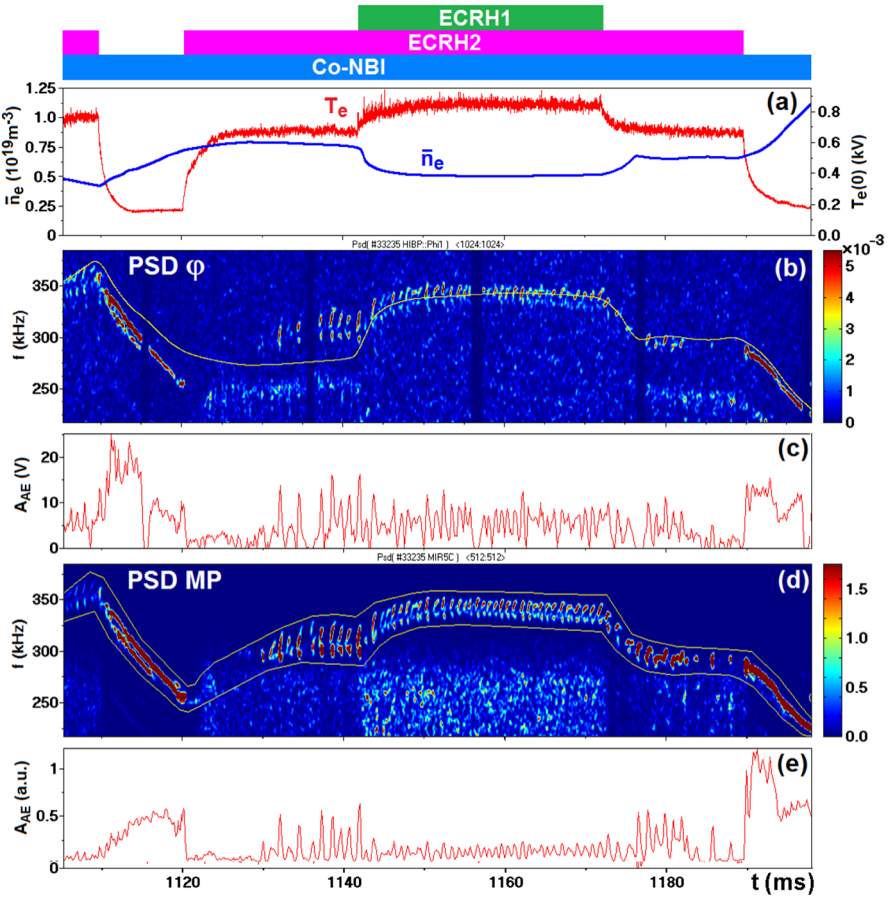

Fig. 29 ECRH power effect on the NBI-induced AE (shot #33235, $P_{NBI}=0.55$ MW, $P_{ECRH1}=P_{ECRH2}=240$ MW). **a** Time traces of the central electron temperature $T_e(0)$ and line-averaged density $\bar{n}_e$; **b** Power spectrogram of the plasma potential measured by HIBP. Thin yellow line is modelling of AE frequency by Eqs. (1, 2, 3, 21) with $m=1$, $n=2$, $\rho_{AE}=0.96$; **d** Power spectrogram of magnetic fluctuations measured by Mirnov probe (MP); NBI excites AE with steady frequency, ECRH2 transforms AE from steady to chirping form, addition of ECRH1 suppresses electrostatic and magnetic components of AE as evidenced by HIBP (**c**) and MP (**e**) (Melnikov et al. 2018a)

profile redistribution due to the EC current drive or redistribution of T_e, caused by ECRH, so redistribution of conductivity and plasma current, even minor one, always existing in the stellarator. Recent experiments shows that counter-ECCD seems to be an effective tool of Alfvénic modes control (actuator) in TJ-II (Nagaoka et al. 2013; Yamamoto et al. 2020; Cappa et al. 2021), however, the problem of AE stabilization is still not resolved issue, which requires further intense researches.

9 Summary

Here we summarize more than 10 years of the direct application of the heavy ion beam probing (HIBP) to study Alfvén eigenmodes (AEs) in TJ-II.

With this diagnostic, for the first time, NBI-induced AEs were characterized simultaneously by oscillations in plasma potential φ, density n_e and magnetic potential measured in the plasma core in both steady-frequency and chirping forms and their radial localizations were determined.

Local amplitudes of the AE modes on φ is as large as up to 100 V, and on n_e is about several percent. Poloidal rotation velocity of AEs found to be as large as several dozens of km/s, AE-induced turbulent particle flux may exceed the one driven by the broadband turbulence at the same frequency range up to a factor of 10. It was shown that turbulent particle flux is an individual characteristics of the AE, it can be directed outwards, inwards, or the mode can have zero flux.

2D map of the AE amplitudes demonstrates poloidally asymmetric (ballooning) character of potential perturbation.

In TJ-II, the radial localization and extent of AEs does not show spatial evolution during a plasma discharge despite the density and rotational transform ι dynamics, however, the AE frequency f_{AE} is drastically sensitive to iota as $f_{\mathrm{AE}} \sim k_{\parallel} = |n - m\iota|$, showing the f_{AE} variation up to seven times during the shot, and also the Alfvénic density dependence $f_{\mathrm{AE}} \sim {n_e}^{-1/2}$.

AE frequency dynamics down to geodesic acoustic mode (GAM) frequency is observed with iota variation. The AE frequency dynamics is described by the analytical model based on the local single mode AE dispersion relation for the cylindrical cold plasma. This model is valid for the whole set of the observed AEs in TJ-II, including the case of $k_{\parallel} \sim 0$, when GAM contribution to AE frequency becomes significant.

AE transformation from continuous frequency to the chirping form caused by iota variation and also by moderate ECRH power (one gyrotron) switch-on was found. When the additional ECRH power (one more gyrotron) is applied, chirping AEs are suppressed.

Chirping modes can demonstrate the significant change of localization and frequency during the burst cycle.

Comparison of the frequency, spatial location and absolute values of potential and density perturbation with numerical simulations by AE3D, FAR3D and CONTY allows us to identify various AEs as HAE and GAE with typical mode numbers $m < 6$ and $n < 9$.

10 Outlook

Alfvén modes study with HIBP takes an important part of the TJ-II research program (Hidalgo et al. 2022). Among the near-term issues there are following key topics: investigation of AE-broadband turbulence interplay, the long-range toroidal

correlations for AE with two HIBP systems, AE dynamics in regimes with normal and improved confinement induced by injection of fuel and impurity pellets, edge polarization (biasing) (Hidalgo et al. 2004) effect on AE, mechanisms for AE stabilization by ECRH/ECCD, comprehensive validation of gyro-fluid and gyrokinetic models.

One of the most crucial direction of the future work is more extended and direct comparison of the modelling and observation, just started, as presented above and in Rakha et al. (2018, 2019) and Ghiozzi et al. (2022) but still has a lot of open issues. Among them, there are the explanation of the permanent radial location with strong variation of the mode frequency in the experiments with plasma current variation, modelling of the chirping mode patterns and characteristics, transition from steady frequency to chirping mode and back, evolution of the chirping mode location during one burst.

Diagnostic complex of TJ-II and HIBP itself has a potential for further development for the foreseen AE study. AEs were mostly found in TJ-II with two main AE diagnostics: magnetic probes (MP) and HIBP. There are also important contributions from Langmuir probes, bolometry and Doppler reflectometry limited by the sensitivity and observation areas of each diagnostic. Dominating majority of AEs are observed simultaneously with HIBP and MP, in addition, many of them are also observed with multichannel bolometry. But there are also some marginal exceptions, where some modes are invisible for some of diagnostics, like mode labeled as $f_{\mathrm{AE}}^{(3)}$ in the Fig. 8, which would be very interesting and important to investigate in the future.

HIBP application for the densities above 3×10^{19} m^{-3} needs special efforts to increase the initial beam current (Bondarenko et al. 2004; Krupnik et al. 2008) to overcome the beam attenuation along the trajectories. The further study of the high-density plasmas caused by pellet injection (McCarthy et al. 2019) erects the plan for the getting stronger initial beam current with finer focusing.

The MP system is also under the development for AE study, the implementation of the additional MP arrays is expected to provide poloidal and toroidal AE mode numbers (Hidalgo et al. 2022).

Acknowledgements The authors warmly acknowledge the long-term trilateral collaboration with our colleagues from TJ-II team, CIEMAT, Madrid, Spain, leaded by Carlos Hidalgo, and HIBP group from Kharkov Institute of Physics and Technology, Kharkov, Ukraine, leaded by L.I. Krupnik and A.S. Kozachek. We are grateful to our Japanese colleagues T. Ido, A. Shimizu, S. Oshima, S. Yamamoto and K. Nagaoka for joint experiments in TJ-II as well as theoreticians and computer modellers B.N. Breizman (USA), A. Könies (Germany), S.E. Sharapov (UK), D.A. Spong (USA) and J. Varela (Spain), and many other colleagues for assistance in experiments and fruitful discussions. AVM is partly supported by the Competitiveness Program of NRNU MEPhI.

References

H. Alfvén, Existence of electromagnetic-hydrodynamic waves. Nature **150**, 405–4066 (1942)

K. Appert, R. Gruber, F. Troyon, J. Vaclavik, Excitation of global eigenmodes of the Alfven wave in Tokamaks. Plasma Phys. **24**(9), 1147 (1982). https://doi.org/10.1088/0032-1028/24/9/010

E. Ascasibar, D. Alba, D. Alegre et al., Overview of recent TJ-II stellarator results. Nucl. Fusion **59**, 112019 (2019). https://doi.org/10.1088/1741-4326/ab205e

H.L. Berk, C.J. Boswell, D. Borba et al., Explanation of the JET $n = 0$ chirping mode. Nucl. Fusion **46**, S888 (2006). https://doi.org/10.1088/0029-5515/46/10/S04

I.S. Bondarenko, A.A. Chmuga, N.B. Dreval et al., Installation of an advanced heavy ion beam diagnostic on the TJ-II stellarator. Rev. Sci. Instrum. **72**, 583 (2001). https://doi.org/10.1063/1.1310593

I.S. Bondarenko, A.A. Chmyga, N.B. Dreval, S.M. Khrebtov, A.D. Komarov, A.S. Kozachek, L.I. Krupnik, L.G. Eliseev, A.V. Melnikov, S.V. Perfilov, Heavy ion beam injection systems for fusion plasma diagnostics. Rev. Sci. Instrum. **75**, 1835–1837 (2004). https://doi.org/10.1063/1.1699515

B.N. Breizman, S.E. Sharapov, Major minority: energetic particles in fusion plasmas. Plasma Phys. Controlled Fusion **53**, 054001 (2011). https://doi.org/10.1088/0741-3335/53/5/054001

B.N. Breizman, M.S. Pekker, S.E. Sharapov, Plasma pressure effect on Alfvén cascade eigenmodes. Phys. Plasmas **12**, 112506 (2005). https://doi.org/10.1063/1.2130692

V.I. Bugarya, A.V. Gorshkov, S.A. Grashin et al., Electric potential and toroidal and poloidal rotation velocities of a tokamak plasma. JETP Lett. **38**(7), 404–408 (1983)

V. Bugarya, A. Gorshkov, S. Grashin et al., Measurements of plasma column rotation and potential in the TM-4 tokamak. Nucl. Fusion **25**, 1707–1717 (1985). https://doi.org/10.1088/0029-5515/25/12/001

A. Cappa, J. Varela, D. Lopez-Bruna et al., Stability analysis of TJ-II stellarator NBI driven Alfvén eigenmodes in ECRH and ECCD experiments. Nucl. Fusion **61**, 066019 (2021). https://doi.org/10.1088/1741-4326/abf74b

F. Castejon, A. Aguilera, E. Ascasibar et al., Influence of magnetic well on electromagnetic turbulence in the TJ-II stellarator. Plasma Phys. Control. Fusion **58**, 094001 (2016). https://doi.org/10.1088/0741-3335/58/9/094001

F. Castejón, D. Alegre, A. Alonso et al., 3D effects on transport and plasma control in the TJ-II stellarator. Nucl. Fusion **57**, 102022 (2017). https://doi.org/10.1088/1741-4326/aa7691

G.D. Conway, A.I. Smolyakov, T. Ido, Geodesic acoustic modes in magnetic confinement devices. Nucl. Fusion **62**, 013001 (2022). https://doi.org/10.1088/1741-4326/ac0dd1

A. Di Siena, T. Görler, E. Poli, R. Bilato, H. Doerk, A. Zocco, Resonant interaction of energetic ions with bulk-ion plasma micro-turbulence. Phys. Plasmas **26**, 052504 (2019a). https://doi.org/10.1063/1.5087203

A. Di Siena, T. Görler, E. Poli et al., Electromagnetic turbulence suppression by energetic particle driven modes. Nucl. Fusion **59**, 124001 (2019b). https://doi.org/10.1088/1741-4326/ab4088

P.H. Diamond, S.-I. Itoh, K. Itoh, T.S. Hahm, Zonal flows in plasma—a review. Plasma Phys. Control. Fusion **47**, R35 (2005). http://iopscience.iop.org/0741-3335/47/5/R01

Y. Dnestrovskij, A. Melnikov, L. Krupnik, I. Nedzelskij, Development of heavy ion beam probe diagnostics. IEEE Trans. Plasma Sci. **22**, 310–331 (1994). https://doi.org/10.1109/27.310637

L. Eliseev, A. Melnikov, S. Perfilov, C. Hidalgo, Two point correlation technique for the measurements of poloidal plasma rotation by heavy ion beam probe. Plasma Fusion Res. **7**, 2402064 (2012). https://doi.org/10.1585/pfr.7.2402064

L.G. Eliseev, A.V. Melnikov, S.E. Lysenko et al., Evaluation of turbulent particle flux by heavy ion beam probe in the T-10 Tokamak. Plasma Fusion Res. **13**, 3402106 (2018). https://doi.org/10.1585/pfr.13.3402106

L.G. Eliseev, A.V. Melnikov, E. Ascasibar et al., Experimental observation of the geodesic acoustic frequency limit for the NBI-driven Alfvén eigenmodes in TJ-II. Phys. Plasmas **28**, 072510 (2021). https://doi.org/10.1063/5.0049225

A. Fasoli, C. Gormenzano, H.L. Berk et al., Progress in the ITER physics basis. Chapter 5: Physics of energetic ions. Nucl. Fusion **47**, S264–S284 (2007). https://doi.org/10.1088/0029-5515/47/6/S05

M. Garcia-Munoz, S.E. Sharapov, M.A. Van Zeeland et al., Active control of Alfvén eigenmodes in magnetically confined toroidal plasmas. Plasma Phys. Controlled Fusion **61**, 054007 (2019). https://doi.org/10.1088/1361-6587/aaef08

A.G. Ghiozzi, M. Mantsinen, P. Pastells, D.A. Spong, A.V. Melnikov, S.E. Sharapov, Modeling of Alfvén cascades in the TJ-II stellarator with STELLGAP and AE3D codes, 48th EPS Conference on Plasma Physics, June 27, to July 1, 2022, Maastricht, Rep. P2b.121. https://epsplasma2022.eu

N.N. Gorelenkov, S.D. Pinches, K. Toi, Energetic particle physics in fusion research in preparation for burning plasma experiments. Nucl. Fusion **54**, 125001 (2014). https://doi.org/10.1088/0029-5515/54/12/125001

M.P. Gryaznevich, J. Stöckel, G. Van Oost et al., Contribution of joint experiments on small tokamaks in the framework of IAEA coordinated research projects to mainstream fusion research. Plasma Sci. Technol. **22**, 055102 (2020). https://doi.org/10.1088/2058-6272/ab6d4d

W.W. Heidbrink, Basic physics of Alfvén instabilities driven by energetic particles. Phys. Plasmas **15**, 055501 (2008). https://doi.org/10.1063/1.2838239

C. Hidalgo, M.A. Pedrosa, N. Dreval et al., Improved confinement regimes induced by limiter biasing in the TJ-II stellarator. Plasma Phys. Control. Fusion **46**, 287–297 (2004). https://doi.org/10.1088/0741-3335/46/1/018

C. Hidalgo, E. Ascasíbar, D. Alegre et al., Overview of the TJ-II stellarator research programme towards model validation in fusion plasmas. Nucl. Fusion **62**, 042025 (2022). https://doi.org/10.1088/1741-4326/ac2ca1

R. Jiménez-Gómez, A. Könies, E. Ascasíbar et al., Alfvén eigenmodes measured in the TJ-II stellarator. Nucl. Fusion **51**, 033001 (2011). https://doi.org/10.1088/0029-5515/51/3/033001

F. Jobes, R. Hickok, A direct measurement of plasma space potential. Nucl. Fusion **10**, 195–197 (1970). https://doi.org/10.1088/0029-5515/10/2/015

Ph.O. Khabanov, L.G. Eliseev, A.V. Melnikov et al., Density profile reconstruction using HIBP in ECRH plasmas in the TJ-II stellarator. J. Instrum. **14**, C09033 (2019). https://doi.org/10.1088/1748-0221/14/09/C09033

L.I. Krupnik, A.D. Komarov, A.S. Kozachek, A.V. Melnikov, I.S. Nedzelskiy, High-intensity alkali ion sources for plasma diagnostics. IEEE Trans. Plasma Sci. **36**, 1536–1544 (2008). https://doi.org/10.1109/TPS.2008.927381

P. Liu, X. Wei, Z. Lin, G. Brochard, G.J. Choi, W.W. Heidbrink, J.H. Nicolau, G.R. McKee, Regulation of AEs by microturbulence in fusion plasmas. Phys. Rev. Lett. **128**, 185001 (2022). https://doi.org/10.1103/PhysRevLett.128.185001

D. López-Bruna, F. Castejón, T. Estrada, J.A. Romero, J.A. Jiménez, E. Ascasíbar and the TJ-II Team, Effects of Ohmic current in the TJ-II stellarator. Nucl. Fusion **44**, 645 (2004). https://doi.org/10.1088/0029-5515/44/5/008

Many authors, IEEE Trans. Plasma. Sci. **22** (4), 287–490 (1994). https://doi.org/10.1109/27.310635

K.J. McCarthy, N. Panadero, S.K. Combs et al., The impact of fast electrons on pellet injection in the stellarator TJ-II. Plasma Phys. Control. Fusion **61**, 014013 (2019). https://doi.org/10.1088/1361-6587/aae038

A.V. Melnikov, Applied and fundamental aspects of fusion science. Nat. Phys. **12**(5), 386 (2016). https://doi.org/10.1038/nphys3759

A. Melnikov, Evolution of heavy ion beam probing from the origins to study of symmetric structures in fusion plasmas. Symmetry **13**(8), 1367 (2021). https://doi.org/10.3390/sym13081367

A.V. Melnikov, I.S. Bondarenko, S.L. Efremov et al., HIBP diagnostics on T-10. Rev. Sci. Instrum. **66**, 317 (1995). https://doi.org/10.1063/1.1146427

A.V. Melnikov, V.A. Vershkov, L.G. Eliseev et al., Investigation of geodesic acoustic mode oscillations in the T-10 tokamak. Plasma Phys. Control. Fusion **48**, S87–S110 (2006). https://doi.org/10.1088/0741-3335/48/4/S07

A.V. Melnikov, L.G. Eliseev, R. Jiménez-Gómez et al., Study of Alfvén eigenmodes in the TJ-II stellarator. Plasma Fusion Res. **5**, S2019 (2010a). https://doi.org/10.1585/pfr.5.S2019

A.V. Melnikov, L.G. Eliseev, R. Jiménez-Gómez et al., Internal measurements of Alfvén eigenmodes with heavy ion beam probing in toroidal plasmas. Nucl. Fusion **50**, 084023 (2010b). https://doi.org/10.1088/0029-5515/50/8/084023

A.V. Melnikov, L.G. Eliseev, R. Jiménez-Gómez et al., Study of Alfvén eigenmodes in the TJ-II stellarator. Plasma Fusion Res. **5**, S2019 (2010c). https://doi.org/10.1585/pfr.5.S2019

A.V. Melnikov, C. Hidalgo, L.G. Eliseev et al., Plasma potential and turbulence dynamics in toroidal devices (survey of T-10 and TJ-II experiments). Nucl. Fusion **51**, 083043 (2011). https://doi.org/10.1088/0029-5515/51/8/083043

A.V. Melnikov, L.G. Eliseev, E. Ascasibar et al., Alfvén eigenmodes properties and dynamics in the TJ-II stellarator. Nucl. Fusion **52**, 123004 (2012). https://doi.org/10.1088/0029-5515/52/12/123004

A.V. Melnikov, M. Ochando, E. Ascasibar et al., Effect of magnetic configuration on frequency of NBI-driven Alfvén modes in TJ-II. Nucl. Fusion **54**, 123002 (2014). https://doi.org/10.1088/0029-5515/54/12/123002

A.V. Melnikov, J.M. Barcala, L.I. Krupnik et al., Control and data acquisition for dual HIBP diagnostics in the TJ-II stellarator. Fusion Eng. Des. **96–97**, 724 (2015). https://doi.org/10.1016/j.fusengdes.2015.01.015

A.V. Melnikov, L.G. Eliseev, E. Ascasíbar et al., Transition from chirping to steady NBI-driven Alfvén modes caused by magnetic configuration variations in the TJ-II stellarator. Nucl. Fusion **56**, 076001 (2016a). https://doi.org/10.1088/0029-5515/56/7/076001

A.V. Melnikov, L.G. Eliseev, F. Castejón et al., Study of NBI-driven chirping mode properties and radial location by the heavy ion beam probe in the TJ-II stellarator. Nucl. Fusion **56**, 112019 (2016b). https://doi.org/10.1088/0029-5515/56/11/112019

A.V. Melnikov, L.G. Eliseev, S.E. Lysenko, M.V. Ufimtsev, V.N. Zenin, Study of interactions between GAMs and broadband turbulence in the T-10 tokamak. Nucl. Fusion **57**, 15001 (2017a). https://doi.org/10.1088/1741-4326/aa796c

A.V. Melnikov, L.I. Krupnik, L.G. Eliseev et al., Heavy ion beam probing—diagnostics to study potential and turbulence in toroidal plasmas. Nucl. Fusion **57**, 072004 (2017b). https://doi.org/10.1088/1741-4326/aa5382

A.V. Melnikov, L.I. Krupnik, E. Ascasibar et al., ECRH effect on the electric potential and turbulence in the TJ-II stellarator and T-10 tokamak plasmas. Plasma Phys. Control. Fusion **60**, 084008 (2018a). https://doi.org/10.1088/1361-6587/aac97f

A.V. Melnikov, E. Ascasibar, A. Cappa et al., Detection and investigation of chirping Alfvén eigenmodes with heavy ion beam probe in the TJ-II stellarator. Nucl. Fusion **58**, 082019 (2018b). https://doi.org/10.1088/1741-4326/aabcf8

A.V. Melnikov, L.G. Eliseev, J.M. Barcala et al., 2D distributions of potential and density mean-values and oscillations in the ECRH and NBI plasmas at the TJ-II stellarator. Plasma Phys. Control. Fusion **64**, 054009 (2022). https://doi.org/10.1088/1361-6587/ac5b4c

A.V. Melnikov. Electric potential in toroidal plasmas. Springer Nature, Switzerland (2019). https://doi.org/10.1007/978-3-030-03481-8

A.V. Melnikov, C. Hidalgo, A.A. Chmyga et al., Plasma potential measurements by the heavy ion beam probe diagnostic in fusion plasmas: biasing experiments in the TJ-II stellarator and T-10 tokamak. Fusion Sci. Technol. **46**, 299–311 (2004). https://doi.org/10.13182/FST04-A568

A.V. Melnikov, A. Alonso, E. Ascasíbar, et al., Plasma potential evolution study by HIBP diagnostic during NBI experiments in the TJ-II stellarator. Fusion Sci. Technol. **51**, 31–37 (2007). https://doi.org/10.13182/FST07-A1284

A.V. Melnikov, M.A. Drabinskiy, L.G. Eliseev, et al., Heavy ion beam probe design and operation on the T-10 tokamak. Fusion Eng. Design **146**, Part A, 850 (2019). https://doi.org/10.1016/j.fusengdes.2019.01.096

K. Nagaoka, T. Ido, E. Ascasíbar et al., Mitigation of NBI driven Alfvén eigenmodes by electron cyclotron heating in the TJ-II stellarator. Nucl. Fusion **53**, 072004 (2013). https://doi.org/10.1088/0029-5515/53/7/072004

N. Nakajima, C.Z. Cheng, M. Okamoto, High-n helicity induced shear Alfvén eigenmodes. Phys. Fluids B **4**, 1115–1121 (1992). https://doi.org/10.1063/1.860119

A. Rakha, M.J. Mantsinen, A.V. Melnikov, et al., Modelling of Alfvén cascades in NBI heated stellarator plasmas, in 45th EPS Conference on Plasma Physics, 2–6 July 2018, Prague, Czech Republic, ECA, vol. 42A, Rep. P4.1004. http://ocs.ciemat.es/EPS2018PAP/pdf/P4.1004.pdf

A. Rakha, M.J. Mantsinen, A.V. Melnikov, et al., Modelling of beam-driven Alfvén modes in TJ-II plasmas. Nucl. Fusion **59**, 056002 (2019). https://doi.org/10.1088/1741-4326/ab0030

G.A. Riggs, S. Nogami, M. Koepke et al., Bispectral analysis of broadband turbulence and geodesic acoustic modes in the T-10 tokamak. J. Plasma Phys. **87**, 885870301 (2021). https://doi.org/10.1017/S0022377821000490

J. Sánchez, D. Alegre, A. Alonso et al., Dynamics of flows and confinement in the TJ-II stellarator. Nucl. Fusion **53**, 104016 (2013). https://doi.org/10.1088/0029-5515/53/10/104016

J. Sánchez, D. Alegre, A. Alonso et al., Transport, stability and plasma control studies in the TJ-II stellarator. Nucl. Fusion **55**, 104014 (2015). https://doi.org/10.1088/0029-5515/55/10/104014

G.A. Sarancha, L.G. Eliseev, A.V. Melnikov, P.O. Khabanov, N.K. Kharchev, Identification of zonal flows and their spatial localization in the TJ-II stellarator. JETP Lett. **116**(2), 96–102 (2022). https://doi.org/10.31857/S1234567822140051

R. Sharma, P.O. Khabanov, A.V. Melnikov et al., Measurements of 2D poloidal plasma profiles and fluctuations in ECRH plasmas using the heavy ion beam probe system in the TJ-II stellarator. Phys. Plasmas **27**, 062502 (2020). https://doi.org/10.1063/1.5142996

D.A. Spong, R. Sanchez, A. Weller, Shear Alfvén continua in stellarators. Phys. Plasmas **10**, 3217–3224 (2003). https://doi.org/10.1063/1.1590316

D.A. Spong, E. D'azevedo, Y. Todo, Clustered frequency analysis of shear Alfvén modes in stellarators. Phys. Plasmas **17**, 022106 (2010). https://doi.org/10.1063/1.3313818

D.A. Spong, M.A. Van Zeeland, W.W. Heidbrink, X. Du, J. Varela, L. Garcia, Y. Ghai, Nonlinear dynamics and transport driven by energetic particle instabilities using a gyro-Landau closure model. Nucl. Fusion **61**, 116061 (2021). https://doi.org/10.1088/1741-4326/ac2990

K. Toi, F. Watanabe, T. Tokuzawa et al., Observation of reversed-shear Alfvén eigenmodes excited by energetic ions in a helical plasma. Phys. Rev. Lett. **105**, 145003 (2010). https://doi.org/10.1103/PhysRevLett.105.145003

K. Toi, K. Ogawa, M. Isobe, M. Osakabe, D.A. Spong, Y. Todo, Energetic-ion-driven global instabilities in stellarator/helical plasmas and comparison with tokamak plasmas. Plasma Phys. Control. Fusion **53**, 024008 (2011). https://doi.org/10.1088/0741-3335/53/2/024008

M.A. Van Zeeland, W.W. Heidbrink, S.E. Sharapov et al., Electron cyclotron heating can drastically alter reversed shear Alfvén eigenmode activity in DIII-D through finite pressure effects. Nucl. Fusion **56**, 112007 (2016). https://doi.org/10.1088/0029-5515/56/11/112007

H. Weisen, A.V. Melnikov, S.V. Perfilov, S.E. Lysenko, On the possibility of using a heavy ion beam probe for local poloidal flux measurements in a tokamak. Fusion Sci. Technol. **59**(2), 418–426 (2011). https://doi.org/10.13182/FST11-A11656

N. Winsor, J.L. Johnson, J.M. Dawson, Geodesic acoustic waves in hydromagnetic systems. Phys. Fluids **11**(11), 2448–2450 (1968). https://doi.org/10.1063/1.1691835

S. Yamamoto, K. Nagasaki, K. Nagaoka et al., Effect of ECH/ECCD on energetic-particle-driven MHD modes in helical plasmas. Nucl. Fusion **60**, 066018 (2020). https://doi.org/10.1088/1741-4326/ab7f13